Title

35Cl(n,x) Cross Section Measurement

Author

Nagel, Tyler

Publication Date

2024

Peer reviewed|Thesis/dissertation

^{35}Cl(n,x) Cross Section Measurement

By

Tyler Scott Nagel

A dissertation submitted in partial satisfaction of the

requirements for the degree of

Doctor of Philosophy

in

Engineering - Nuclear Engineering

in the

Graduate Division

of the

University of California, Berkeley

Committee in charge:

Professor Lee Bernstein, Chair
Professor Barbara Jacak
Professor Massimiliano Fratoni

Spring 2024

^{35}Cl(n,x) Cross Section Measurement

Tyler Scott Nagel

Abstract

^{35}Cl(n,x) Cross Section Measurement

by

Tyler Scott Nagel

Doctor of Philosophy in Engineering - Nuclear Engineering

University of California, Berkeley

Professor Lee Bernstein, Chair

Neutron induced reactions on Chlorine, especially ^{35}Cl, have wide relevance across the nuclear science spectrum. The $^{35}\mathrm{Cl}(n,p_0)^{35}\mathrm{S}$ channel is particularly vital to the design of Molten Chloride Fast Reactors (MCFR) as it impacts core reactivity through neutron loss in the Chlorine based carrier salt. However, until 2019, very little experimental data existed for the relevant energy range. Secondary γ-ray production data for the $^{35}\mathrm{Cl}(n,p)^{35}\mathrm{S}$ reaction are also needed for national security applications, including active neutron interrogation, yet there is currently no useful experimental data available. Gamma-ray data is also used in space exploration for detecting the isotopic makeup of extraterrestrial environments as well as in oil-well logging. To address these nuclear data needs, measurements of the ^{35}Cl(n,x) reaction cross sections were conducted at Lawrence Berkeley National Laboratory's (LBNL) 88-inch cyclotron.

The nuclear data evaluation process that produces the cross sections used for applications assumes a fixed total (n,x) cross section. The result is that an increase in one channel causes a corresponding decrease in one or more other evaluated channel(s). To address this aspect of nuclear data evaluation we performed a multi-component experiment whose goal was to measure all energetically possible reaction channels instead of using the more common single channel approach. The experiment consisted of three independent parts. First, the energy differential $^{35}\mathrm{Cl}(n,p_0)^{35}\mathrm{S}$ cross section was obtained using a CLYC detector as an active target. Second, energy-differential γ-ray production data for $^{35}\mathrm{Cl}(n,p\gamma)^{35}\mathrm{S}$ and $^{35}\mathrm{Cl}(n,n'\gamma)^{35}\mathrm{Cl}$ were obtained using the GENESIS array. This data was compared against (elsewhere produced) CoH_3 theoretical calculations to inform model predictions as to the relative strength of available reaction channels. Finally, energy-integral ^{35}Cl(n,p) and ^{35}Cl(n,α) cross sections from activation were compared against CoH_3. These allow verification of the inelastic channel strength obtained from the γ-ray data as well as determining the total ^{35}Cl(n,α) channel strength which was not available from the other methods.

Our results identify a $\sim$50% reduction in the magnitude of the $^{35}\mathrm{Cl}(n,p_0)^{35}\mathrm{S}$ cross section

compared to the ENDF/B-VIII.0 evaluation. This result is consistent with a 2020 measurement by Kuvin *et. al.* Comparison of the γ-ray production data to CoH_3 model calculations suggest that the elastic and/or inelastic channels must increase to compensate for the reduction observed in the (n, p_0) channel.

For Missy,

the other member of my *duprass*.

Contents

List of Figures

List of Tables

Acknowledgments

There are two people, without whom, I never could have completed a PhD. The first is my wife Missy. For six long years she supported the two of us while I went to school. And don't forget, during four of those years she was also going to school for her Doctorate while working full time. Without her incredible level of support, this never could have happened. The second person is Dr. Josh Brown. I can say with certainty, without his mentorship and technical assistance, I never could have completed this project.

I would also like to thank other members of the GENESIS Group: Anastasia Georgiadou was vital in many calibration and characterization aspects for the NaCl GENESIS run, Joseph Gordon wrote a significant part of the post-processing code-base used for the GENESIS analysis, Dr. Thibault Laplace was always available when I had random questions, and Christopher Brand developed the STOF array which was necessary for this work. Additionally, I would like to thank Dr. Jon Batchelder and Grant Mills for their work on the activation part of the experiment. And finally, my advisor, Dr. Lee Bernstein. Despite his incredibly busy schedule he made time every week, and sometimes more, to meet with me and help in any way he could.

Chapter 1

Introduction

1.1 Molten Chloride Fast Reactors

Many modern, advanced reactor designs strive to increase efficiency, safety, and reliability, while simultaneously decreasing proliferation risk and radioactive waste by exploring exotic fuels and coolants. One such reactor type is the Molten Chloride Fast Reactor (MCFR). The MCFR is a fast spectrum reactor in which molten fuel is mixed with a Chlorine-based salt, forming a salt-fuel eutectic which acts as both the fuel and the primary coolant [25]. High operating temperatures serve to increase thermal efficiency while keeping the fuel in a molten state. Use of molten fuel not only makes meltdown irrelevant, but it has the added economic benefit of not requiring the fabrication of costly fuel assemblies. The addition of a natural circulation decay heat removal system ensures the the reactor is "walk-away safe". The fast neutron spectrum reduces long-lived Actinide production while incorporating a flexible fuel cycle. Some designs, such as that by TerraPower LLC, only require enriched uranium upon initial startup; the makeup feed is depleted Uranium [14]. Proliferation issues such as online reprocessing or on-going enrichment ("breed and burn") are not required for the MCFR. [58]

Nuclear reactors achieve and maintain criticality through a very careful control of the neutron production and loss rates. The key to any nuclear reactor is the fission chain reaction. Prompt neutrons, those neutrons produced immediately following fission, make up the vast majority of neutrons in the system. A smaller, but equally important source of neutrons, is from the β-delayed neutron emission of neutron-rich fission fragments. These are called delayed neutrons and serve to keep the time-rate-of-change of the reaction rate controllable. Sources of neutron loss include engineered losses such as absorption in control rods or burnable poisons. Undesirable sources of neutron loss include leakage from the reactor as well as absorption in structural materials or coolant (the carrier salt for the case of the MCFR).

For a fast reactor in which there is little neutron thermalization, the neutron balance can

be roughly described by the following differential equation [22],

$$\frac{1}{v}\frac{d\phi}{dt} = \nu\Sigma_f\phi - \Sigma_a\phi + D\nabla^2\phi \tag{1.1}$$

where ϕ is the neutron flux, v is the neutron speed, ν is the number of prompt neutrons per fission event, Σ_f and Σ_a are the macroscopic fission and absorption cross sections respectively, and D is the diffusion constant. This equation is known as a "one-group" equation since all neutron are assumed to have the same energy. Setting the derivative to zero and including a scale factor, k, the balance becomes

$$0 = \frac{1}{k}\nu\Sigma_f\phi - \Sigma_a\phi + D\nabla^2\phi. \tag{1.2}$$

If the production rate is greater than the loss rate $\left(\frac{dn}{dt} > 0\right)$, then k must be greater than one to keep the right hand side equal to zero. The opposite is true if the production rate is less than the loss rate. The scale factor k, called the multiplication factor, represents the criticality state of the reactor: supercritical for $k > 1$, critical for $k = 1$, and subcritical for $k < 1$.

The Chlorine enrichment question

The neutron energy spectrum the fuel experiences in an MCFR is a rough Gaussian centered at about 200 keV with a width of about 600 keV FWHM. An example is shown in Figure 1.1 [45]. In this energy range, neutron loss through (n,p), (n,γ) and (n,α) on ^{35}Cl is significant. On the other hand, ^{37}Cl has little to no (n,p), (n,γ) or (n,α) cross section in this energy range [10]. Unfortunately, natural Chlorine is about 75% ^{35}Cl and 25% ^{37}Cl. This suggests that enrichment of the Chlorine in ^{37}Cl may be needed in the design of an MCFR. The ENDF/B-VIII.0 cross sections for these reactions are shown in Figure 1.2.

A 2016 study by Fratoni [45] exposed the sensitivity of MCFR criticality (i.e impact on the infinite multiplication factor k_∞) to changes in the evaluated cross section library and explored how these changes can be reproduced by varying the Chlorine enrichment. The work consisted of SERPENT simulations of an MCFR infinite unit cell for two different versions of ENDF: ENDF/B-VII.0 and ENDF/B-VII.1. Both simulations were conducted for 15% Uranium enrichment and a temperature of 900 K. Table 1.1 lists the results. The relatively small change of -0.00839 b for the ^{35}Cl(n,p) cross section resulted in a 5200 per cent mille (pcm) increase in k_∞ (k_∞ is the multiplication factor assuming an infinitely sized reactor).

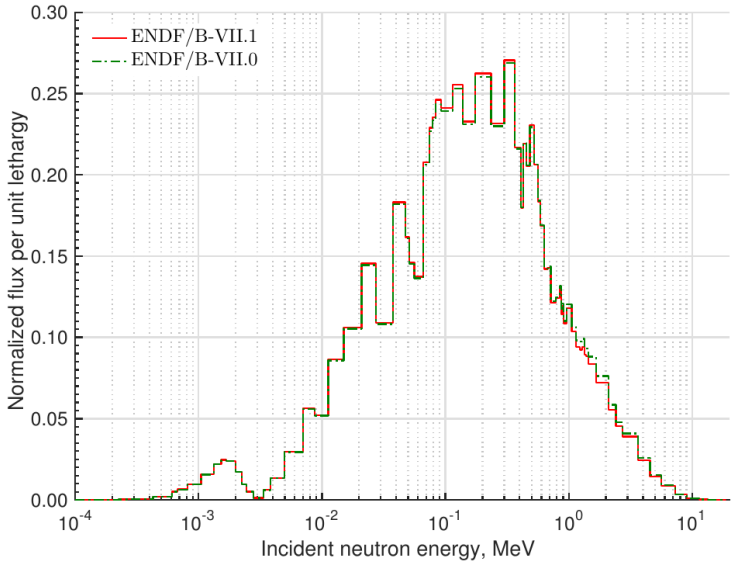

Figure 1.1: Simulated MCFR energy spectrum. Reproduced with permission from [45].

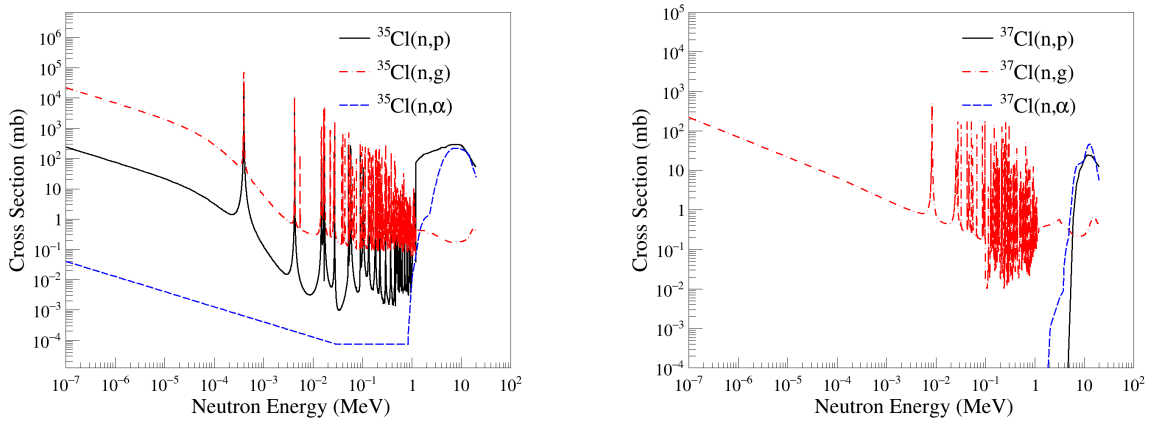

(a) ^{35}Cl (b) ^{37}Cl

Figure 1.2: ENDF/B-VIII.0 Cross Sections for (n,p), (n,γ), and (n,α) on ^{35}Cl and ^{37}Cl.

This increase in k_∞ could also be achieved with the ENDF/B-VII.0 library by increasing the Chlorine enrichment. Figure 1.3 shows how k_∞ increases with enrichment. The black dashed line represents the k_∞ for the ENDF/B-VII.1 library and natural Chlorine. The solid red line is the k_∞ for the ENDF/B-VII.0 library for various levels of enrichment. The two cases are equivalent at an enrichment of 50%. These results imply that if the cross sections for neutron absorbing channels in ^{35}Cl are sufficiently high, the carrier salt must be enriched

Quantity	ENDF/B-VII.0	ENDF/B-VII.1	Difference
k_∞	1.06789 ± 0.00023	1.11989 ± 0.00021	+0.05200
(n,p) Effective Cross Section	0.01947	0.01109	-0.00839
(n,γ) Effective Cross Section	0.00245	0.00246	+0.00001

Table 1.1: Impact of ENDF library on k_∞ for an MCFR. Reproduced with permission from [45].

in ^{37}Cl to compensate for the the loss in reactivity. For this reason, accurate values for the $^{35}\mathrm{Cl}(n, x)$ reaction cross sections are needed.

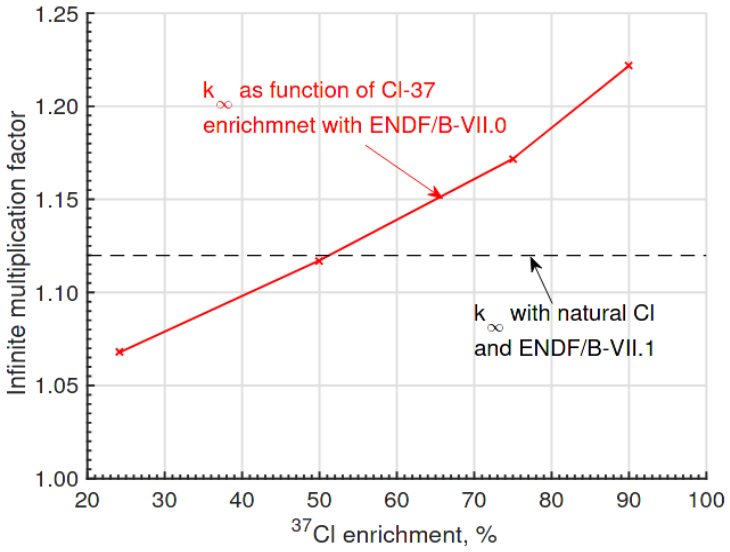

Figure 1.3: Enrichment effects on k_∞ in an MCFR. Reproduced with permission from [45] [sic].

1.2 Active neutron interrogation

Active neutron interrogation uses secondary γ-ray emissions to determine the isotopic composition of complex materials. This technique has applications across the national security spectrum: from controlled substance detection such as explosives, narcotics, or special nuclear material, to arms control/treaty verification. It is also used in space exploration for detecting the isotopic makeup of extraterrestrial environments as well as in oil-well logging [47].

Chlorine is present in a vast array of everyday and exotic substances, from radiation detectors to household chemicals, to narcotics. Despite its ubiquity, Chlorine has received little attention from the nuclear data community. The lack of data for this important element was identified by a multi-laboratory (ORNL, LBNL, LANL, LLNL) working group tasked with assessing modeling and nuclear data needs for active neutron interrogation [47]. The group tabulated their finding as a set of elements grouped by priority tier. Chlorine was placed in the second, or "follow-up" tier.

1.3 The state of nuclear data

Measurements of ^{35}Cl$(n,p)^{35}$S

There have been two dozen measurements of the ^{35}Cl$(n,p)^{35}$S cross sections since the 1940's. However, seventeen of these were done for thermal and epithermal neutron energies, a region not relevant to the MCFR. Another three experiments, performed in the late 1960's, used the DT fusion energy of 14 MeV. This energy is again not relevant for the MCFR. This leaves just four experiments in the relevant energy range.

Popov 1961

Popov et al. [61] measured the ^{35}Cl(n,p) cross section from 26 ev - 7.4 keV via a slowing-down time in lead method. The authors used a liquid CCl(4) or C(3)Cl(6) target with an effective thickness of 1×10^{21} Cl nucl/cm^2 and a Zn-S(Ag) powder scintillation detector.

Koehler 1991

Koehler et al. [37] measured the ^{35}Cl(n,p) cross section from 27.5 meV - 146 keV at the Los Alamos Neutron Scattering Center (LANSCE) at LANL. Neutrons produced via spallation were directed on a natural potassium-chloride target with a thin aluminum backing. A ^{6}Li target was also placed downstream of the potassium-chloride target, allowing the ^{35}Cl(n,p) cross section to be determined relative to the ^{6}Li(n,α)t reaction. In this way, the ^{35}Cl(n,p) cross section can be determined up to a constant factor that accounts for the difference in detector efficiencies between the two detectors. The authors assumed that the ^{35}Cl(n,p) and ^{6}Li(n,α)t were well known at thermal energies. The ratio of these two yielded a correction factor that was applied to the higher energy experimental data.

Batchelder 2019

Batchelder et al. [4] measured the energy-integrated ^{35}Cl(n,p) and ^{35}Cl(n,α) cross sections from 2.42-2.74 MeV using activation. Neutrons with an energy range of 2.18-2.74 MeV were produced via DD fusion neutrons using the High Flux Neutron Generator [3] at the University of California, Berkeley. A series of NaCl pellets, co-loaded with natural Ni foils,

were placed at various angles with respect to the beam. The ^{35}Cl$(n,p)^{35}$S and ^{35}Cl$(n,\alpha)^{32}$P cross sections were determined relative to the reference ^{58}Ni$(n,p)^{58}$Co cross section. Their results for the (n,α) cross section agreed well with the evaluated data libraries, but the (n,p) values were a factor of 3 to 5 times lower than the evaluated libraries. The experimental values were not only much lower than expected but showed a clear resonance structure, indicating a resolved resonance model rather than a statistical Hauser-Feshbach model is more appropriate in this energy range.

Kuvin 2020

Kuvin et al. [39] performed measurements of the partial, energy-differential (n,p_i) and (n,α_i) cross sections from 0.6-6 MeV via the in-beam observation of protons and neutrons emitted from a thin target during neutron irradiation. In this experiment, neutrons from the WNR spallation source [40] at Los Alamos National Laboratory (LANL) were directed to a NaCl target and charged particles produced were measured using the Low Energy (n,z) (LENZ) system. Their work confirms the large overestimation of the (n,p) cross section in evaluated libraries as well as a resonance behavior up to 3 MeV.

Figure 1.4 shows the evaluated ENDF/B-VIII.0 ^{35}Cl(n,p)^{35}S cross section [10] along with four previous measurements: Batchelder [4], Kuvin [39], Koehler [37], and Popov [61]. The yellow histogram represents a modeled MCFR neutron flux in normalized flux per unit lethargy [45]. The figure shows a clear lack of experimental data in the region where the MCFR flux peaks. The two recent experiments, Batchelder and Kuvin, agree with a reduction in the magnitude compared to ENDF, but disagree in their absolute magnitudes. This discrepancy is highlighted in Figure 1.5, where the Batchelder *et al.* data is seen to be roughly half that of Kuvin *et al.*. To help adjudicate these discrepancies, the ^{35}Cl$(n,p_0)^{35}$S cross section was measured in the energy range of 2.02 to 7.46 MeV.

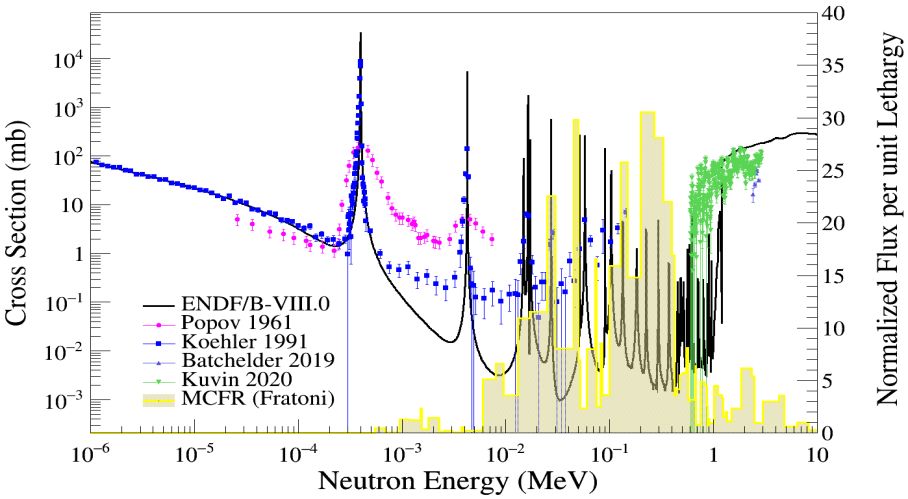

Figure 1.4: ENDF/B-VIII.0 evaluated cross section along with relevant experimental data. The solid black line is the ENDF evaluated cross section and the colored points are the measured data. The yellow overlay is a putative MCFR neutron spectrum.

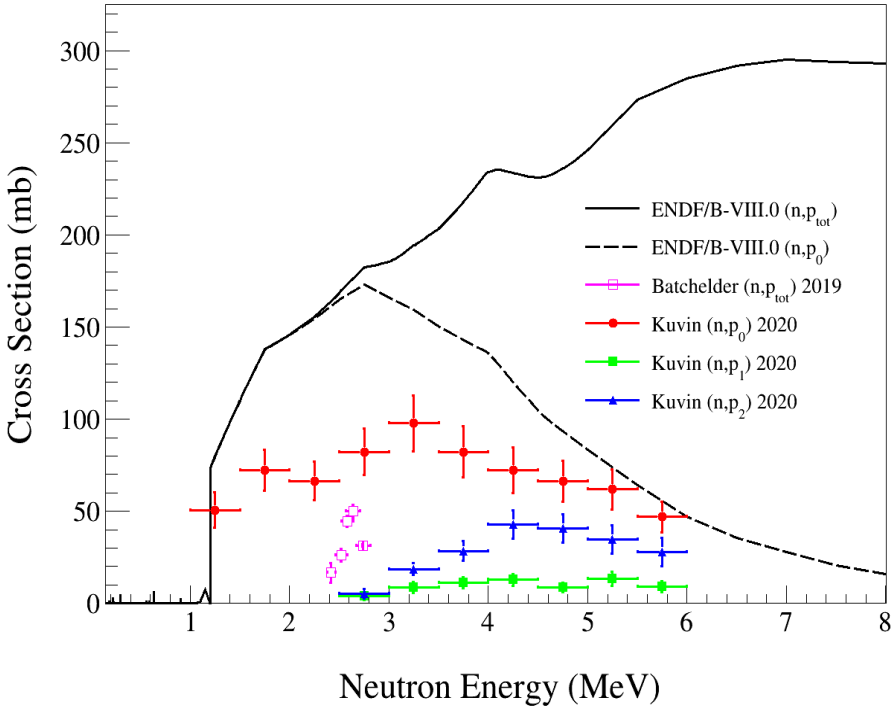

Figure 1.5: Another view of ENDF/B-VIII.0 evaluated cross section along with relevant experimental data. This view highlights the discrepancy in recent measurements.

Chapter 2

Theory

This dissertation is primarily focused on presenting the results of a three-part experiment performed at the LBNL 88-Inch cyclotron. However, the interpretation of these measurements are in turn dependent on both the structure of the ^{35}Cl+n system and the reaction mechanisms by which they were formed. This dependence on fundamental nuclear science is central to the nuclear data evaluation process which produces the values used in the energy and national security applications described in the introduction. In the interest of completeness, this chapter provides a short description of the underlying nuclear structure and reaction models underlying the evaluation process.

2.1 Nuclear Structure Models

Liquid drop model

The oldest of all nuclear models, the liquid drop model (LDM), views the nucleus as the nuclear corollary to the classical liquid drop. That is, it is a macroscopic object with properties such as a well defined surface, constant density, incompressability, surface tension, as well as bulk properties such as temperature. The difference lies in that the particles making up the drop are Fermions, which due to the Pauli Exclusion Principle, causes non-classical effects. Some examples are the large average inter-nucleon distance and the rarity of inter-particle collisions. [50]

Classically, each of the A particles in the drop attract (A-1) others, resulting in $\frac{1}{2}(A-1)$ total interactions. Thus, binding energy per nucleon ($\frac{B(A,Z)}{A}$) should be proportional to the number of nucleons. However, this is not what is observed. For $A > 12$, $\frac{B(A,Z)}{A}$ is fairly constant with an average of ≈ 8 MeV [38]. This saturation property is primarily a result of the short range of the nuclear force: *each nucleon only attracts a limited number of other nucleons*. As the inter-nucleon distance decreases, the kinetic energy rises due to the Heisenberg Uncertainty Principle [38],

$$\Delta p \Delta x \geq \frac{\hbar}{2}. \tag{2.1}$$

At small distances, the kinetic energy overtakes the attractive nuclear potential resulting in a positive total binding energy (i.e. non-binding). At large distances, where the kinetic energy is small, the nuclear potential is small due to its finite range. Thus, the total binding energy is zero and once again is non-binding. The result is that only a small range of inter-nucleon distances result in a total attractive potential [50]. The result is nuclei with features reminiscent of a liquid drop: constant density, incompressability, and a sharp surface.

The liquid drop concept can be expanded into a semi-empirical model that fairly accurately represent the shape of the $\frac{B(A,Z)}{A}$ curve. The most popular formulation is the Bethe-Weizsacker equation [38],

$$B(A,Z) = \overbrace{a_v A}^{\text{volume}} + \overbrace{a_s A^{2/3}}^{\text{surface}} - \overbrace{a_c \frac{Z(Z-1)}{A^{1/3}}}^{\text{Coulomb}} - \overbrace{a_{sym} \frac{(A-2Z)^2}{A}}^{\text{symmetry}} + \overbrace{\delta}^{\text{pairing}} \tag{2.2}$$

where, a_v etc. are experimentally determined constants.

The first term is the volume term. It accounts for binding energy due to all of the nucleon-nucleon interactions. It is proportional to A since the volume is proportional to A,

$$V = \frac{4}{3} r^3 = \frac{4}{3} (r_0 A^{1/3})^3 \propto A. \tag{2.3}$$

The second term is the surface term. It accounts for surface tension of the drop; nucleons at the surface have fewer neighbors and therefore contribute less to the total binding energy. It is proportional to $A^{2/3}$ since the surface area is proportional to $A^{2/3}$,

$$SA = 4\pi r^2 = 4\pi (r_0 A^{1/3})^2 \propto A^{2/3}. \tag{2.4}$$

The third term is the Coulomb term. It accounts for the Coulomb repulsion between the protons. It is proportional to $\frac{Z^2}{A^{1/3}}$ since the number of proton-proton interactions is proportional to Z^2 and each interaction has an energy that is proportional to r (i.e. $A^{1/3}$). Therefore, the total Coulomb energy is proportional to $\frac{Z^2}{A^{1/3}}$.

The fourth term is the symmetry term. It accounts for neutron or proton excesses. This term is best described with the Fermi Gas Model [19]. Consider three separate non-relativistic Fermi gases: one of protons (Z), one of neutrons (N), and one of protons and

neutrons (A). A given particle has energy $\epsilon(k)$ and momentum k. The highest occupied energy level is the Fermi energy ϵ_F. Let k_F^p be the Fermi-momentum for the proton system, k_F^n be the Fermi-momentum for the neutron system, and k_F be the Fermi-momentum for the combined system. For particles in a box of side length L, the particle number is

$$Z \text{ or } N = 8\pi(L/2\pi)^3 \int k^2 dk \tag{2.5}$$

and the energy (E) for each system is

$$E = 8\pi(L/2\pi)^3 \int \epsilon(k) k^2 dk. \tag{2.6}$$

The total energy (E_t) of the neutron system (N) plus the proton system (Z) is

$$E_t = \frac{8\pi(L/2\pi)^3}{2m} \left(\int_0^{k_F^p} k^4 dk + \int_0^{k_F^n} k^4 dk \right) = \frac{4\pi(L/2\pi)^3}{5m} \left((k_F^p)^5 + (k_F^n)^5 \right)$$

where, $\epsilon(k) = k^2/2m$ is the non-relativistic energy momentum relation. For the combined system (A), the total particle number

$$A = 16\pi(L/2\pi)^3 \int k^2 dk. \tag{2.7}$$

Plugging in the equation for the combined system (A) into that for the proton system (Z),

$$k_F^p = \left(\frac{A - \Delta}{A} \right)^{1/3} k_F, \qquad k_F^n = \left(\frac{A + \Delta}{A} \right)^{1/3} k_F$$

where Δ = N - Z, gives a total energy in terms of A and Δ,

$$E_t = \frac{4\pi(k_F)^5(L/2\pi)^3}{5m} \left(\left(\frac{A - \Delta}{A} \right)^{5/3} + \left(\frac{A + \Delta}{A} \right)^{5/3} \right).$$

Expanding in powers of Δ/A and keeping only the first two non-zero terms,

$$E_t = \frac{4\pi(k_F)^5(L/2\pi)^3}{5m}\left(2 + \frac{10}{9}(\frac{\Delta}{A})^2\right).$$

The total energy is the kinetic energy plus an extra term that is zero if and only if N = Z. Combining constants into one empirical parameter, the second term is desired symmetry correction to the binding energy,

$$E_{sym} = a_{sym}\frac{(A-2Z)^2}{A}. \tag{2.8}$$

The final term in the Bethe-Weizsacker formula is the pairing term. Its form depends on the symmetry of N and Z [38],

$$\delta = \begin{cases} +a_p A^{-3/4} & even-even \\ -a_p A^{-3/4} & odd-odd \\ 0 & odd-even \end{cases}. \tag{2.9}$$

The pairing effect refers to the preferred coupling of two nucleons in a given j-orbital to a spin-zero state. It has manifold effects in nuclear structure including odd-even effects in binding energy and the presence of low-lying 2^+ states in even nuclei [50]. In a given j-orbital there can be up to $j(j+1)$ nucleons. These nucleons each have a spin of j and can couple their spins as

$$j_{tot} = j_1 \otimes j_2 \otimes \cdots \otimes j_{j(j+1)}. \tag{2.10}$$

The lowest energy configuration will be the one in which spin-0 pairs form. From a semi-classical standpoint, the lowest energy, most strongly bound, configuration is one in which the nucleons orbit with the smallest separation distance. Two nucleons in co-planer orbits can align (j_{max}), or anti-align (j_{min}) their spins. In the (j_{max}) case, the nucleons orbit in the same direction and on the extreme opposite sides of orbit (the separation maintained by the Pauli Principle). In the (j_{min}) case, the nucleons orbit in opposite directions and thus their time-averaged distance is less, resulting in a more tightly bound configuration [12]. Other couplings are possible and these represent excited states . Nuclei can be excited by breaking the pair and coupling spins to a value other than 0, with an energy cost of about 2 MeV [38].

The Spherical Shell Model

The mean field approximation

The A-nucleon Schrödinger Equation cannot be solved exactly. A particularly popular approximation is the *mean field approximation* which converts the strongly interacting particles into non-interacting quasi-particles, [56]

$$H = T + V = \sum_{i=1}^{A} \frac{-\hbar^2}{2m}\nabla_i^2 + \sum_{\substack{i,j=1 \\ i<j}}^{A} v(\vec{r}_i, \vec{r}_j). \tag{2.11}$$

Adding and subtracting a single particle potential,

$$H = T + V = \overbrace{\sum_{i=1}^{A} \frac{-\hbar^2}{2m}\nabla_i^2 + \sum_{i=1}^{A} v(\vec{r}_i)}^{H_{mf}} + \overbrace{\sum_{\substack{i,j=1 \\ i<j}}^{A} v(\vec{r}_i, \vec{r}_j) - \sum_{i=1}^{A} v(\vec{r}_i)}^{V_{res}}. \tag{2.12}$$

The total Hamiltonian is now split into a *mean field Hamiltonian* H_{mf} and a (hopefully small) *residual interaction* V_{res}

$$H = H_{mf} + V_{res}. \tag{2.13}$$

The A-nucleon wavefunction Ψ can be separated into a product of single particle wavefunctions ϕ. This can be done since the qausi-particles are non-interacting and thus their operators commute,

$$\Psi(\vec{r}_1, \vec{r}_2, ..., \vec{r}_A) = \phi_{\alpha 1}(\vec{r}_1)\phi_{\alpha 2}(\vec{r}_2)...\phi_{\alpha A}(\vec{r}_A). \tag{2.14}$$

This gives A identical one-nucleon Schrödinger Equations

$$h(\vec{r})\phi_\alpha(\vec{r}) = \epsilon_\alpha \phi_\alpha(\vec{r}) \tag{2.15}$$

where

$$h(\vec{r}) = \frac{-\hbar^2}{2m}\nabla^2 + V(\vec{r}) \tag{2.16}$$

and a total energy of

$$E = \sum_{i=1}^{A} \epsilon_{\alpha_i}. \tag{2.17}$$

The solution of the many particle Schrödinger Equation is thus a product of single particle wavefunctions obtained by solving a one-nucleon Schrödinger Equation for an external potential well. In this way the mean field concept has turned the complicated many nucleon problem into a simple one nucleon one. The above analysis made no supposition as to the form of the potential well. There are two general ways to arrive at a form for this potential. The first, or *phenomenological method*, is to simply choose a mathematical form. Common choices include the harmonic oscillator and the Woods-Saxon. The second option is called the *Hartree-Fock method* and involves using the variational method to arrive at a potential by iteration. [50]

The phenomenological method

Two candidate potentials that have easily calculable solutions and reproduce the first three magic numbers are the infinite square well and the quantum harmonic oscillator (QHO) [38]. The QHO spectrum has the following properties:

1. The shells are evenly spaced (harmonic) [38].
2. The QHO has a very high degree of symmetry (SU(3)), resulting in very highly degenerate levels [41].
3. The QHO Hamiltonian commutes with rotations and thus the spectroscopic factors (s,p,d, etc.) are good quantum numbers [41].
4. The QHO Hamiltonian commutes with parity and thus each shell has a definite parity. This parity oscillates according to $\pi = (-1)^l$ [38].
5. The QHO reproduces the first three magic numbers, 2, 8, 20. However it fails for higher magic numbers [38].
6. The number of particles in each shell is the sum of particles in each orbital. The number of particles in each orbital follows $n = 2(2l + 1)$ [38].

A more realistic spectrum is obtained by choosing a more realistic form for the potential. A popular choice is the Woods-Saxon (WS) potential, defined as [50]:

$$V^{ws}(r) = -V_0 \left(1 + e^{\left(\frac{r-R_0}{a}\right)}\right)^{-1} \tag{2.18}$$

with

$$R_0 = r_0 A^{1/3} \quad V_0 \approx 50\ MeV \quad a \approx 0.5\ fm \quad r_0 \approx 1.2\ fm$$

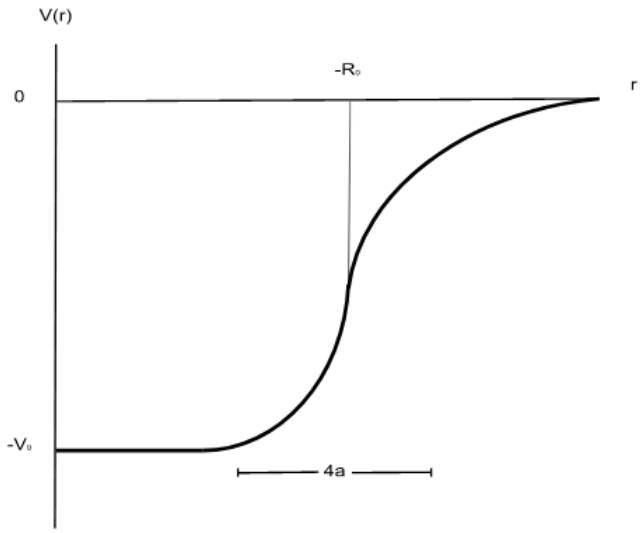

Figure 2.1: A Woods-Saxon Potential. Reproduced from [50]

The Woods-Saxon potential has less symmetry than the QHO and thus there is a breakage of some of the degeneracy as one moves from the QHO to the WS. The l-orbitals in a given shell are no longer degenerate but the $2(2l+1)$ degeneracy within each orbital remains since the WS is still rotationally invariant and thus energy cannot depend on orientation. The previously degenerate orbitals separate and arrange themselves with lowest l on top and highest l on the bottom by action of the centrifugal potential. Higher l orbitals have a larger centrifugal potential and so are more bound, moving their energies down.

In order to achieve reproduction of all magic numbers a *spin-orbit* term must be added to the potential. Its general form is [38],

$$V_{so}(r)\vec{L} \cdot \vec{S}.$$

Various forms for V_{so} exist; one possible choice that makes V_{so} reach a maximum near the nuclear surface is [50],

$$V_{so}(r) = \lambda \frac{1}{r}\frac{dV}{r}. \tag{2.19}$$

The addition this new $\vec{L}\cdot\vec{S}$ term requires a new basis. The $\vec{L}\cdot\vec{S}$ term does not commute with either l or s but does commute the J, the generator of overall rotations. It also commutes with the Casimir operators L^2, S^2 and J^2. Thus the new symmetry adapted basis is $\{|nlsjm_j\rangle\}$ [42]. The effect of the spin orbit interaction is to split each l-orbital into a spin-orbit doublets, $l \pm 1/2$, with energy separation [38]

$$\Delta E \propto \langle \vec{L}\cdot\vec{S}\rangle_{j=l+\frac{1}{2}} - \langle \vec{L}\cdot\vec{S}\rangle_{j=l-\frac{1}{2}} = \frac{1}{2}(2l+1)\hbar^2. \tag{2.20}$$

The splitting of levels is a manifestation of further reduction in the symmetry of the Hamiltonian. This energy splitting is linear in l and so higher l orbitals will see a larger splitting. The $l - \frac{1}{2}$ state is always above the $l + \frac{1}{2}$ state due to the attractive nature of the spin-orbit force [50]. As these levels split they cause a shift in the shell gaps. Since the spread in these spin-obit doublets is proportional to l and the highest l orbitals are on the bottom of a given WS shell, sometimes the $l + \frac{1}{2}$ orbital will intrude into the lower shell of opposite parity. These are the so-called *intruder orbitals* [50].

Figure 2.2 graphically illustrates the evolution of nuclear shell gaps as one moves to more realistic nuclear potentials. The models represented are the quantum harmonic oscillator, the Woods-Saxon, and the Woods-Saxon plus spin-orbit. At each stage, new levels emerge (previously degenerate) and shift in energy according to the nature of the potential. The Woods-Saxon plus spin-orbit case is seen to properly reproduce the experimentally observed magic numbers.

2.2 Nuclear Reactions

A typical binary nuclear reaction may be written [52]:

$$A + a \rightarrow B + b. \tag{2.21}$$

Written in this way, A is interpreted as the target nucleus and a as the projectile. A specific combination of particles is referred to as a *partition*. Target A and projectile a together constitute the *entrance partition*. Partitions can be distinguished from *channels*.

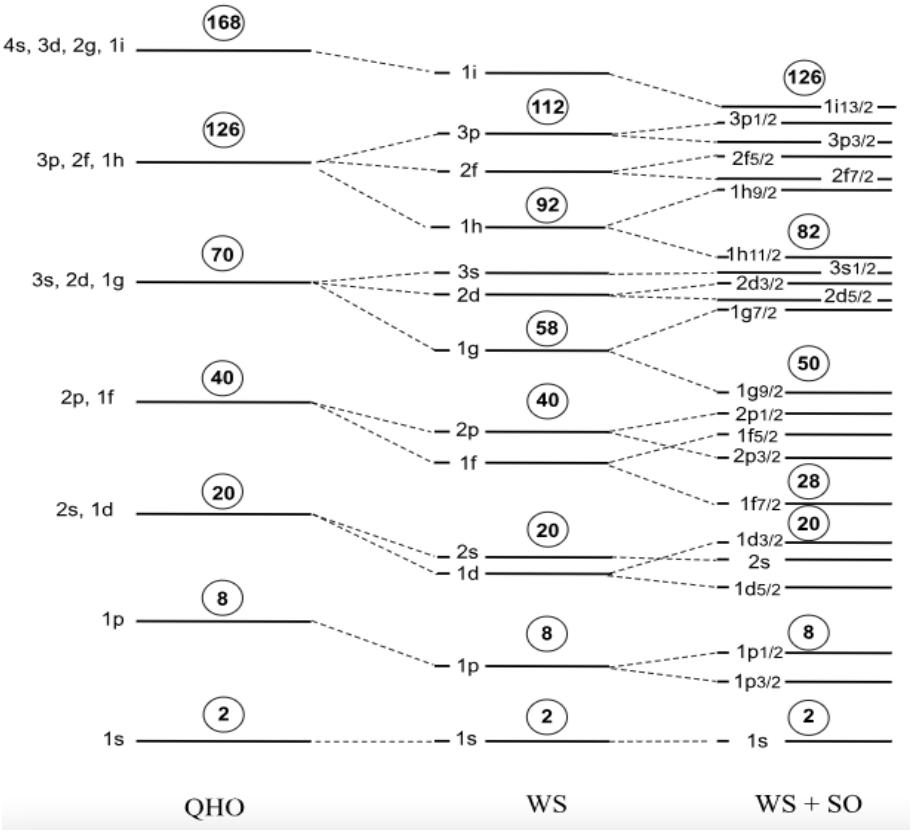

Figure 2.2: Level diagram showing how the magic numbers emerge as the potential is made more realistic. QHO is the quantum harmonic oscillator, WS is the Woods-Saxon, and WS+SO is the Woods-Saxon plus spin-orbit. Image is reproduced and modified from [38]

.

The particles that make up a given partition can exist in various states of excitation; each such possibility is called a *channel*. If both A and a are in their ground states, which is normally the case, then it is referred to as the *entrance channel*. The *exit partition* consists of residual nucleus B and ejectile b. The exit partition is subdivided into (possibly many) *exit channels*, in which each channel corresponds to a specific set of excitations of B and b [52]. It is common practice to refer to partitions as channels (e.g. *the inelastic channel*).

The total cross section is the sum of all possible exit partitions for a given entrance channel. More intuitively, it is the total likelihood that the incident particle will interact with the target and do "something". Measurement of the total cross section via a so-called *transmission experiment* is one of the simplest cross section measurements possible and this type of experiment has been a favorite since the early days of the field. Transmission experiments consist of measuring the loss in fluence of a particle beam after it passes though

a thin target [52]. The drop in fluence is the total number of reactions that took place, though we can't say what the reactions were. Because these experiments are very simple, they provide a reliable, rigorous bound on the total cross section. Nuclear physics and engineering applications typically require knowledge of individual reaction channels, not just the total cross section. Some channels may be very important while others may be relatively unimportant. Which are important and which are not (if any) depend on the application. Extracting information about a specific channel requires an experiment that can resolve this channel out of the background of competing channels.

For typical laboratory energies of a few keV to a few hundred MeV, observations of nuclear reactions fall into three general categories: compound, direct, and pre-equilibrium [29].

Direct Nuclear Reactions

Direct reactions are those that only involve a few degrees of freedom. Typically, only a few nucleons are involved and they tend to be those near the nuclear surface. Simple reasoning suggests that direct reactions are more important for higher incident energies. As energy rises, the incident particle's wavelength shortens until it is on the same scale as an individual nucleon [38]. Thus, the projectile interacts with one nucleon only. Direct reactions have the following features [38]:

1. *Energy distribution of emitted particles is discrete.* Since direct reactions interact with specific configuration states, the energy spectra of emitted particles show a series of narrow peaks.

2. *Direct reactions are fast.* Since only a couple nucleons are involved, the time for a direct reaction is similar to the nuclear transit time of 10^{-22} seconds.

3. *Direct nuclei remember how they were formed.* The probability of the nucleus decaying via a given channel is highly dependent on the reactants used to create it.

4. *The differential cross section is a strong function of angle.* The few nucleon, non-equilibrium nature of direct reactions produces an angle-differential cross section that varies strongly with angle. The distribution tends to be periodic and reminiscent of diffraction.

Compound Nuclear Reactions

Compound reactions are those that proceed through a well defined intermediate state, $a + X \rightarrow C^* \rightarrow Y + b$ [38]. The compound nucleus is highly excited and the incoming energy has been shared equally among all nucleons. Particle emission occurs when one nucleon

eventually acquires enough energy to overcome the binding energy and escape the nucleus. This is analogous to the evaporation of water. Compound reactions thus involve many degrees of freedom and are described statistically. Compound reactions are more common with low energy projectiles and medium to heavy nuclei. Low energy projectiles will have wavelengths on the same scale as the nuclear size, thus they will interact with all nucleons simultaneously. Compound reactions have the following features [38]:

1. *Energy distribution of emitted particles is continuous.* Since the particles emitted from the compound nucleus are "boiled off", their energy spectrum resembles a Maxwellian distribution. The spectrum can be used to determine the *temperature* of the nucleus.

2. *Compound reactions are slow.* It takes a while for one nucleon to gain enough energy from random collisions to escape, typically about $10^{-18} - 10^{-16}$ seconds. This is long considering that a 5 MeV neutron would take only about 10^{-22} seconds to cross a nucleus of radius 5 fm.

3. *Compound nuclei forget how they were formed.* Since the energy and angular momentum are shared stochastically among all nucleons, there is no longer any way to tell how it was formed. All we know is the total energy and angular momentum. Thus, the probability of the compound nucleus decaying via a given channel does not depend on the reactants used to create it.

4. *The differential cross section is roughly independent of angle.* Again, since the energy and angular momentum are shared stochastically among all nucleons there is no preferred direction to emit the particle and they are emitted (roughly) isotropically (in the COM-frame). In other words, the angle differential cross section is constant.

Pre-equilibrium Nuclear Reactions

Pre-equilibrium reactions are intermediate to the direct and compound regimes. Here the incoming particle has been absorbed into an intermediate state like a compound nucleus, except particle emission occurs before equilibrium is reached [24]. Thus, the features of pre-equilibrium reactions contain elements from both models.

Nuclear reactions form an extremely complex problem, and such, a purely microscopic analysis is not possible. Any attempt to describe or model nuclear reactions must use simplified mathematical models to reproduce the observations noted above. In general, reaction models can be grouped into three categories: optical model, compound nucleus model, and the pre-equilibrium model. The optical model provides the shape elastic and direct components. It is also used to feed information to the pre-equilibrium and compound models. The compound nucleus model provides the compound elastic, fission, and other compound reaction components [29].

The Optical Model

The elastic scattering of two objects can be described by a static potential that depends only on the nature of the two particles. If the problem is converted to the center-of-mass frame, the problem becomes that of a point particle interacting with a static interaction potential [24]. This is shape elastic scattering. However, colliding nuclei have internal structure and can be excited. Thus, these other possibilities must be included which cannot be described by a real interaction potential. The scattering problem is described by the time-independent Schrödinger equation for a particle of reduced mass μ and optical potential $V_{opt}(\vec{r})$ [24],

$$\left(-\frac{\hbar}{2\mu}\nabla^2 + \overbrace{V(\vec{r}) + iW(\vec{r})}^{V_{opt}}\right)\psi(\vec{r}) = E\psi(\vec{r}). \tag{2.22}$$

The probability density current is,

$$\vec{j} = \frac{\hbar}{2\mu i}(\psi^*\nabla\psi - \psi\nabla\psi^*). \tag{2.23}$$

Taking the divergence of $\vec{j}$,

$$\nabla\cdot\vec{j} = \frac{\hbar}{2\mu i}(\psi^*\nabla^2\psi - \psi\nabla^2\psi^*) = \frac{1}{\hbar}(\psi^*W\psi - \psi W\psi^*) = \frac{2}{\hbar}\rho(\vec{r})W(r) \tag{2.24}$$

where $\rho(\vec{r})$ is the probability density. This indicates that adding a negative imaginary component ($iW(r)$) to the optical potential will cause a "sink" in the probability current. This loss in current accounts for all non-elastic reactions. This is sometimes called the reaction cross section (σ_r) and is defined as the ratio of the net current to the total incoming current. The net current is obtained by integrating over a surface S. Using the Divergence Theorem,

$$\oint_S \vec{j}\cdot\vec{a} = \int_V (\nabla\cdot\vec{j}(\vec{r}))d^3r = \frac{2}{\hbar}\int_V \rho(\vec{r})W(r)d^3r. \tag{2.25}$$

If the incoming particle is described a plane wave ($\psi = e^{i\vec{k}\cdot\vec{r}}$) the incoming current is,

$$\vec{j}_{inc} = \frac{\hbar\vec{k}}{\mu} = \vec{v}, \tag{2.26}$$

so that the reaction cross section is [24],

$$\sigma_r = \frac{2}{\hbar v} \int_V \rho(\vec{r}) W(r) d^3r. \tag{2.27}$$

In time-independent scattering theory the scattering amplitude is sometimes written as a linear combination of spherical harmonics [43]. This is called the *partial wave expansion*. Essentially, the incident wave is expanded into a series of partial waves where each partial wave has a specific value of angular momentum l [38]. The formalism of this method will not be discussed here, however we will use the concept to obtain a simplified form for the reaction cross section [24],

$$\sigma_r = \frac{\pi}{k^2} \sum_{l=0}^{\infty} (2l+1) T_l \tag{2.28}$$

where, k is the wavenumber, l is the partial-wave angular momentum, and T_l is the transmission coefficient for angular momentum l. The transmission coefficients represent that part of the current that is not reflected from the potential (i.e. transmitted). These will be needed to calculate exit channel probabilities in the compound nucleus model.

Direct reactions in the optical model are handled by the Distorted Wave Born Approximation (DWBA) for spherical nuclei or the couple-channel formalism for deformed nuclei [32]. It is typical in scattering theory to represent the wavefunction for the scattered wave as a product of a spherical wave and an angular function called the scattering amplitude. The scattering amplitude encodes the angular dependence of the scattered wave [43],

$$\psi_{scatt}(r, \theta, \phi) \approx \frac{e^{ikr}}{r} f(\theta, \phi). \tag{2.29}$$

From probability density arguments it can be shown that the differential cross section is simply the square of the scattering amplitude.

$$\frac{d\sigma}{d\Omega} = |f(\theta, \phi)|^2 \tag{2.30}$$

The scattering amplitude can be shown to be proportional to the matrix element between the scattered wave $|k'\rangle$ and the exact solution $|\psi_k\rangle$ [44],

$$f(\theta,\phi) = -\frac{4\pi^2 m}{\hbar^2}\langle k'|V|k\rangle. \tag{2.31}$$

Central to formal descriptions of scattering theory is the Lippmann-Schwinger equation,

$$|\psi_k\rangle = |k\rangle + \hat{G}_{0+}(E)V|\psi_k\rangle \tag{2.32}$$

where, $|\psi_k\rangle$ is the exact solution to the scattering problem, $|k\rangle$ is the incident plane wave, $\hat{G}_{0+}(E)$ is the free-particle outgoing Green's operator and V is the scattering potential. Rearranging for the exact solution $|\psi_k\rangle$ we have,

$$|\psi_k\rangle = \Omega_+(E)|k\rangle \tag{2.33}$$

where, $\Omega_+ = (1 - \hat{G_{0+}})^{-1}$. The operator ω_+ is the Moller scattering operator. Assuming V is small and expanding gives,

$$\Omega_+(E) = 1 + G_{0+}(E)V + G_{0+}(E)VG_{0+}(E)V + ... \tag{2.34}$$

The Lippmann-Schwinger equation now reads,

$$|\psi_k\rangle = |k\rangle + \hat{G}_{0+}(E)V|k\rangle + \hat{G}_{0+}(E)V\hat{G}_{0+}(E)V|k\rangle + ... \tag{2.35}$$

This is known as the Born Series. The scattering amplitude is now,

$$f(\theta,\phi) = -\frac{4\pi^2 m}{\hbar^2}\left[\langle k'|V|k\rangle + \langle k'|V\hat{G}_{0+}(E)V|k\rangle + \langle k'|V\hat{G}_{0+}(E)V\hat{G}_{0+}(E)V|k\rangle + ...\right]. \tag{2.36}$$

Limiting the series at order-n is called the Born Approximation. Analysis in which the incident wave is a plane wave is known as the Plane Wave Born Approximation (PWBA). However, better comparison to experimental data is achieved if the waves are not plane waves, but distorted (DWBA) [24].

Compound Nucleus Model

The compound nucleus model must be invoked when the number and complexity of intermediate states increase to the point where they must be treated statistically. The compound

process is viewed as occurring in two main steps: fusion, in which the incoming particle is absorbed by that target to create a highly excited compound nucleus with energy shared equally by all nucleons and decay step, in which the compound nucleus decays in to any one of a series of exit channels. Based on this the cross section for a reaction from entrance channel a to exit channel b for spin J is written as [24],

$$\sigma^J_{a\to b} = \sigma_F(a)^J G(b)^J \tag{2.37}$$

where $\sigma_F(a)$ is the fusion cross section for channel a and $G(b)^J$ is the decay probability into channel b. By definition,

$$\sigma_F(a)^J = \sum_b \sigma^J_{a\to b} \tag{2.38}$$

and

$$\sum_b G(b)^J = 1. \tag{2.39}$$

The Hamiltonian describing the reaction is time-reversal invariant and thus the partial cross section from $a \to b$ is equal to the time reversed case of $b \to a$ (principle of detailed balance),

$$k_a^2 \sigma^J_{a\to b} = k_b^2 \sigma^J_{b\to a}. \tag{2.40}$$

Substituting this into Equation 2.37 we have,

$$\frac{k_a^2 \sigma_F(a)^J}{G(a)^J} = \frac{k_b^2 \sigma_F(b)^J}{G(b)^J} = const. \tag{2.41}$$

Finally, using the unitarity relation 2.39 we have for the partial cross section,

$$\sigma^J_{a\to b} = k_b^2 \frac{\sigma_F(a)^J \sigma_F(b)^J}{\sum_c k_c^2 \sigma_F(c)^J} \tag{2.42}$$

where c is a dummy index. Interestingly, the partial cross section for a compound nucleus reaction from $a \to b$ can be written purely in terms of fusion cross sections. Equation 2.28

from the optical model gave the reaction cross section, now interpreted as a fusion cross section, in terms of transmission coefficients. The channel cross sections is,

$$\sigma^J_{a\to b} = \frac{\pi}{k_a^2}(2J+1)\frac{T(a)^J T(b)^J}{\sum_c k_c^2 T(c)^J}. \tag{2.43}$$

This is the Hauser-Feshbach equation and is the backbone of statistical reaction model codes such as CoH_3 [32].

Chapter 3

Experimental Design

3.1 Introduction

In order to address the problems in calculating criticality in an MCFR discussed in Chapter 1, we designed an experiment to measure the ^{35}Cl$(n,p)^{35}$S cross section. The nuclear data evaluation process that produces the cross sections used for applications, such as in the design of an MCFR, assumes a fixed total (n,x) cross section. The result is that a change in one channel causes a corresponding change in one or more other evaluated channel(s). This concept is described graphically in Figure 3.1. Competing neutron induced reaction channels in the MCFR energy range include ^{35}Cl(n,n)^{35}Cl, ^{35}Cl(n,n'γ)^{35}Cl, ^{35}Cl(n,γ)^{36}Cl, and ^{35}Cl(n,α)^{32}P. All of these channels, not just the (n,p), are important to the reactor designer. For this reason, our experiment was designed to measure as many channels as possible. This was accomplished with a three-part experiment consisting of an activation portion, a γ-spectrometry portion, and an active target portion. All three portions of the experiment were carried out at the Berkeley 88-Inch Cyclotron at Lawrence Berkeley National Laboratory (LBNL).

3.2 Neutron Source

The Berkeley 88-Inch Cyclotron

Built in 1959, the Berkeley 88-Inch Cyclotron is a variable energy, high current, K=140 sector-focused cyclotron. With both heavy and light-ion capabilities, the 88-Inch Cyclotron supports a wide range of nuclear science activities, from nuclear structure and astrophysics, to technology R&D [33]. Accelerated ion beams are created by one of three ions sources and delivered in pulses to one of nine experimental caves.

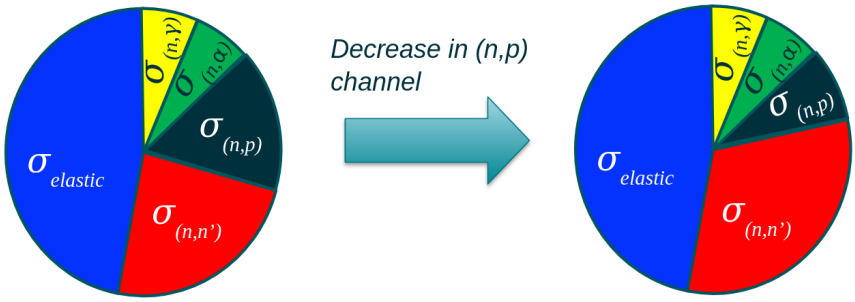

Figure 3.1: Visual representation of total cross section conservation. Any change in one channel necessitates a change in one or more other channels.

Temporal profile

All cyclotrons rely on the same underlying principle: *the revolution frequency of a charged particle moving in a magnetic field is independent of radius or energy.* This is easily shown by equating magnetic and centrifugal forces ($F_{magnetic} = F_{cent}$) [60],

$$qvB = \frac{mv^2}{r} \therefore \frac{v}{r} \equiv \omega = \frac{qB}{m}, \tag{3.1}$$

where, q, m, v, are the particle's charge, mass, and speed respectively. r is the orbit radius, B is the magnetic field strength, and ω is the angular frequency. Equation 3.1 ignores the relativistic effects present in a K=140 cyclotron. For the work presented in this thesis, $^2H^+$ ions were accelerated to 14 MeV. According to Equation 3.1, cyclotron radio frequency (rf) is a function of particle mass and energy. For our case of 14 MeV deuterons, the rf was 5.907 MHz, corresponding to a pulse period of 169.3 ns. The beam pulse, upon extraction from the cyclotron, contains contributions from several orbits which can result in a wide, multi-modal temporal profile. The profile was optimized by adjusting Dee voltage and septum angle-of-attack.

3.3 Experiment Overview

Figure 3.2 shows a sketch of the experimental setup. On the right is the cyclotron vault and on the left is the Cave 5 experimental area. A neutron beam was created via thick target deuteron breakup (TTDB) on a 5 cm diameter, 3.5 mm thick graphite breakup target. The resulting neutron beam impinged on a 60 cm long copper collimator which served to constrain the angular width of the beam. The collimator is made of six segments, each 10 cm in length

and having a different bore sizes. The borehole radii range from 0.33 cm on the upstream side to 0.6 cm on the downstream side. The cyclotron vault and experimental Cave 5 are separated by a shielding wall consisting of 0.91 m of steel on the Vault side and 1.52 m of concrete on the Cave 5 side. A 10 cm diameter air filled, iron beam pipe penetrates this shielding wall [26]. A Mylar window covers the Vault side opening. Upon exiting the collimator but prior to passing into Cave 5, the neutrons arrive at the first part of the experiment. This is the activation portion, and consisted of a small NaCl target. The ^{35}Cl(n,p) and ^{35}Cl(n,α) reactions produce radioactive ^{35}S and ^{32}P whose decay can be subsequently measured to determine the energy-integrated (n,p) and (n,α) cross sections. This portion is discussed in detail in Chapter 6. Following the activation target, the neutron beam passes through a shielding wall into Cave 5 and arrives at the GENESIS array. GENESIS, the Gamma Energy Neutron Energy Spectrometer for Inelastic Scattering, is an array of organic scintillators and High Purity Germanium (HPGe) detectors for neutron and γ-ray detection respectively [26]. An NaCl target, similar to the one used in the activation part but bigger, was placed in the center of the GENESIS array. From this, γ-ray production yields were determined and compared to theoretical calculations. This portion is discussed in detail in Chapter 5. The third part of the experiment was the active target portion. For this we used a CLYC detector which is a type of inorganic scintillator that contains Chlorine allowing for direct measurement of the energy differential ^{35}Cl(n,p) cross section. This portion is discussed in detail in Chapter 4.

3.4 Neutron Spectrum

STOF

The deuteron breakup process is composed of two effects: direct stripping reaction (nuclear breakup) and dissociation in the coulomb field of the target (Coulombic breakup). Coulombic breakup dominates when the heavy targets and nuclear breakup dominates for lighter targets (e.g. Carbon) and at high energies [8] In TTDB the target is sufficiently thick to stop all protons. The neutron spectrum resulting from deuteron breakup is a complex problem that is not well understood for incident deuteron energies $\leq$65 MeV and must be measured experimentally [8].

The neutron flux profile was measured using the Scattering Time-Of-Flight (STOF) system [28]. Located at the back of the cave behind GENESIS and the CLYC, STOF consists of eight 1" EJ-309 liquid scintillators. A pair of detectors, placed face to face, are placed in the beam line together forming the *target cell*. The other six detectors, designated *scatter cells*, are placed in a circular pattern about a foot behind the scattering cell and in the plane transverse to the beam line. Incoming neutrons elastically scatter off of Hydrogen in the scattering cell and are subsequently detected by one of the detector cells. By measuring the time elapsed between the two events, the outgoing neutron energy can be inferred. The flux

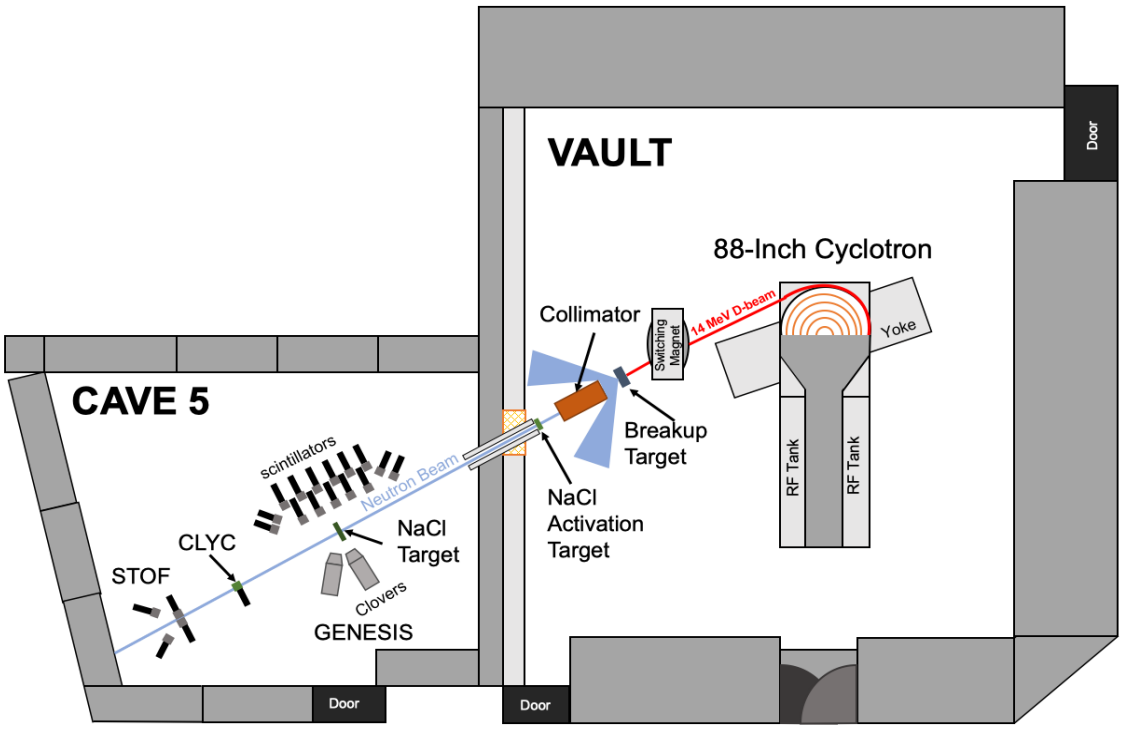

Figure 3.2: Schematic of the experimental layout.

cannot be obtained below 2 MeV due to uncertainty in the detection efficiency. The STOF data for this experiment suffered from a non-linearity in the response above 8 MeV. This prevented an accurate flux shape above 8 MeV from being obtained. However, this feature was not present in other data sets, such as that from an Fe experiment conducted in June of 2021. This experiment also consisted of 14 MeV deuterons on a Carbon target. Thus, the flux shape between the two should be identical, the only difference being in the magnitude resulting from small changes in the experimental setup such as alignment of the collimator. The shape of the NaCl data set was unaffected by non-linearity in the 3-7 MeV region. An integral normalization over this energy range was performed to scale the Fe data to the NaCl magnitude. Figure 3.3 shows the measured neutron flux in units of $neutrons/MeV/str/\mu C$. The red data points indicate the August NaCl data and the black data points are June Fe data that has been scaled to match the NaCl data. The black box indicates the region over which the integral normalization was performed.

Frame overlap

Frame overlap, also called wraparound, is a neutron energy ambiguity phenomenon that results from using a beam that is both broad in energy and cyclic in time. For our experimental conditions of 14 MeV deuterons, the cyclotron had a period of about 170 ns resulting in a

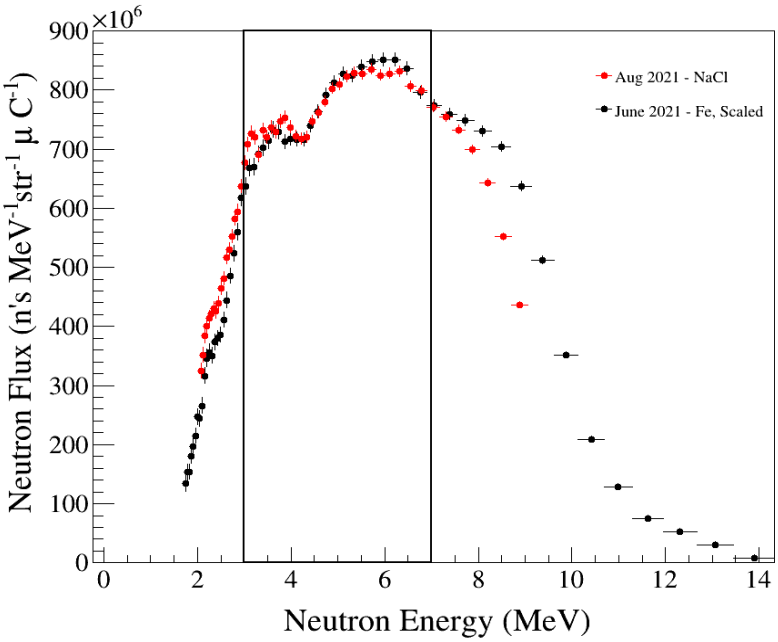

Figure 3.3: Experimental neutron flux as measured by the STOF system. The red data points are the STOF data from this experiment. This data set suffered from non-linearity effects above 7 MeV. The black data points are from a previous Iron experiment which did not suffer any non-linearity issues and has been scaled to match the NaCl data over the 3 - 7 MeV energy range. This region is indicated by the black box.

burst of neutrons every 170 ns. Since each pulse contains neutrons with a wide variation in energy, the high energy neutrons will arrive at the detector with a short time-of-flight (TOF) while the low energy neutrons will arrive with a long TOF. Figures 3.4 and 3.5 depict a visual representation of the frame overlap phenomenon at two different detector flight path lengths. In the figures, the blue square represents the time window during which neutrons from the first pulse can arrive. 170 seconds later, another pulse occurs. Since the fastest neutrons from this pulse arrive before the slowest neutrons from the previous pulse, it is impossible to tell (at least from knowledge of the TOF alone) which pulse they came from. Thus their energy is unknown. All but the first and last pulse in the experiment will have the structure of the red pulse, that is, an overlap at high energy and an overlap at low energy. Since there are countless cycles during the experiment, essentially all pulses have this character.

The wrapped nature of the neutron flux is made apparent by representing it as a 2D histogram of neutron energy vs. time since last *rf*, called the flux matrix. The flux matrix is shown in Figure 3.6. If a horizontal line, representing a specific time since last *rf* value, is drawn over the flux matrix, it will be seen to intersect multiple bands. Therefore, a given

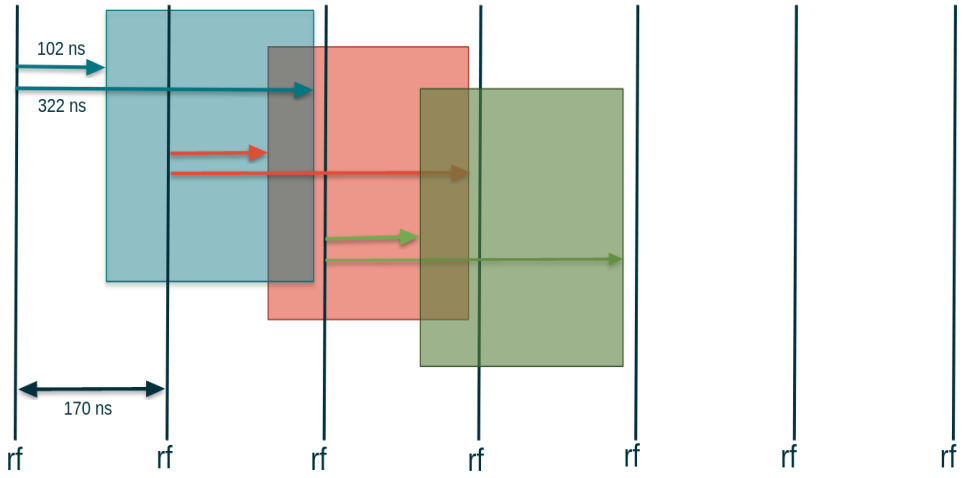

Figure 3.4: Frame overlap diagram for 4.4 m setup

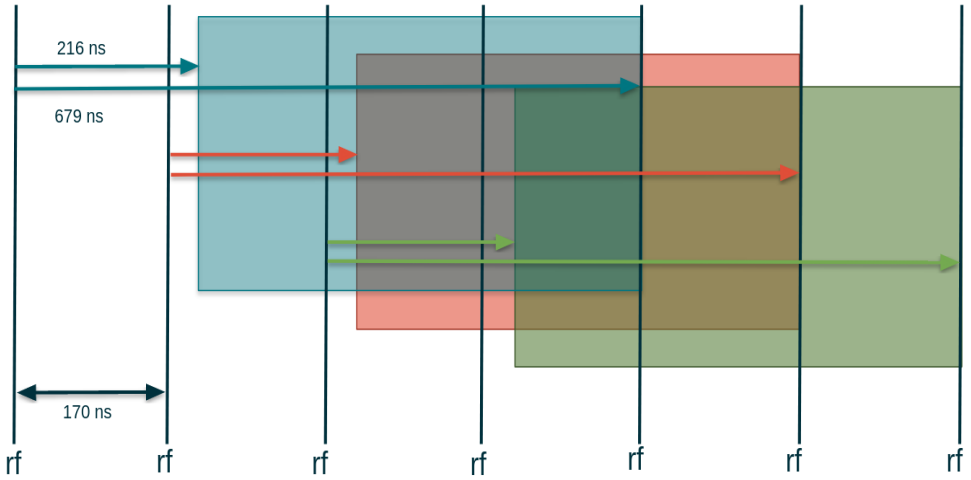

Figure 3.5: Frame overlap diagram for 9.4 m setup

time since last *rf* value corresponds to multiple energies.

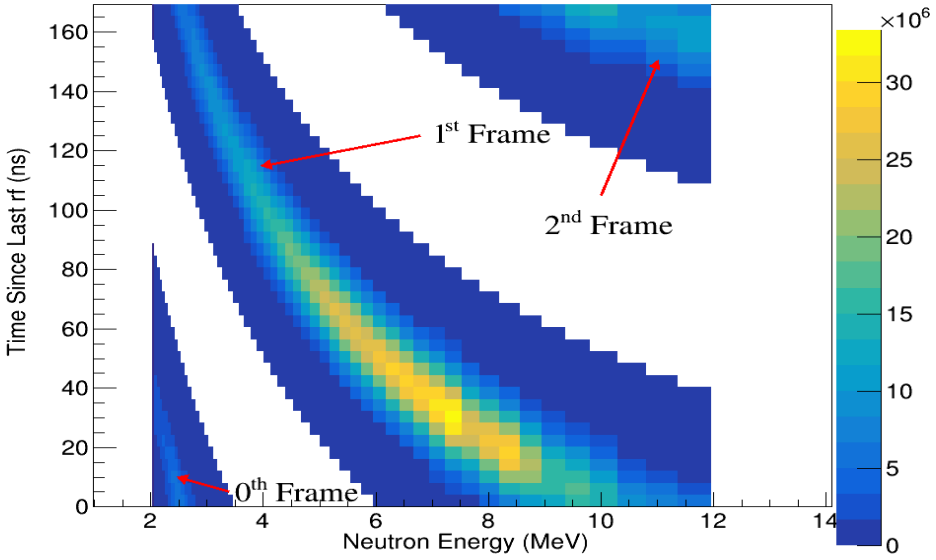

Figure 3.6: STOF Flux matrix. Frame overlap is observed as a series of bands. Viewed in this way, it is clear that a given time-since-last *rf* can correspond to multiple neutron energy values.

Chapter 4

CLYC Analysis and Results

4.1 Introduction

As one of the oldest types radiation detectors still in use, scintillation counters play a vital role in nuclear research activities and associated applications [36]. Despite their ubiquity, scintillators tend to suffer from poor: resolution, proportionality, and sensitivity. [20] A new addition to the family of scintillation materials is the cubic elpasolites. A 2012 Sandia National Laboratory technical report promoting cubic elpasolite crystals as an improvement to previous scintillator chemistries says that they

> hold greater promise due to their high light output, proportionality, and potential for scale-up. The isotropic cubic structure leads to minimal thermomechanical stresses during single-crystal solidification, and eliminates the problematic light scattering at grain boundaries. This class of materials seems clearly destined for important applications in nonproliferation, and they may yield the first large, low-cost gamma spectrometers approaching theoretical energy resolution [20].

Cubic elpasolite materials have the general chemical formula A_2BLnX_6 (A,B = alkali metal; Ln = lanthanide; X = halogen). The most common of the elpasolite scintillators is CLYC (Cs_2LiYCl_6), which has been rising in popularity due to its dual mode use as both a high resolution gamma spectrometer and a neutron detector. The rise in interest is evidenced by a multitude of papers on CLYC pulse shape discrimination [17, 18, 34, 46, 55], scintillation mechanisms [18], response function [18, 9, 17], proton light yield [55], modeling with MCNP [9] and GEANT4 [46].

Neutron sensitivity of CLYC comes from several reactions: primarily the ^{6}Li(n,α)t, ^{35}Cl(n,p), and ^{35}Cl(n,α) reactions.

4.2 Experimental Setup

This experiment used a 25-mm-dia. x 25-mm-h. right circular cylindrical CLYC6 scintillator (i.e., enriched in the ^{6}Li isotope to 95%) from Radiation Monitoring Devices [15] as an active target. Enrichment in ^{6}Li was chosen to enhance the ^{6}Li(n,α)t signal. In this work, measurements were made at two different flight path lengths, a 9.4 m long flight path and a 4.4 m short flight path. The two cases constitute independent data sets. The scintillator crystal was mounted to a 60-mm-dia Hamamatsu H13795-100-Y002 photomultiplier tube [27] with a 1-mm-thick Eljen Ej-560 silicon optical coupling pad [53]. The detector assembly was placed on a tripod to facilitate ease of movement between the two positions as well as alignment in the beam. The detector assembly was placed at a right angle to the beam with the scintillator crystal directly in the beam; this geometry kept the photomultiplier tube largely out of the beam. The detector was centered in the beam by aligning a Huepar 902CG cross line laser level [30] with predetermined beamline reference points on the cave walls.

Data acquisition

Data acquisition was performed with a CAEN DT5725S desktop digitizer [21] with Digital Pulse Processing - Pulse Shape Discrimination firmware (DPP-PSD) [1]. Analog to digital conversion is via a 14-bit, 250 MS/s flash ADC. Samples thus occur every 4 ns with $2^{14} = 16,384$ possibilities making this rate good for medium to fast signals. [21]. CAEN's multi-parametric software, CoMPASS [16], was used to set parameters and record data for the experiment. Relevant acquisition parameters are listed in Table 4.1. Leading edge triggering was chosen due the radically different pulse shapes between neutron-induced and gamma-ray induced pulses observed in the CLYC detector. Timing synchronization with the cyclotron was accomplished by recording cyclotron radio-frequency control signal (rf). CLYC-rf coincidences were built during post-processing. For each event, waveforms consisting of 368 samples (1472 ns) were recorded. Figure 4.1 shows generic signal pulse and the definition of the various settings used.

Pulse shape discrimination

CLYC works well as a dual mode spectrometer due to its good pulse shape discrimination (PSD) characteristics. The digitizer FPGA provides long and short charge integrals (Q_{long}, Q_{short}), corresponding to the "Long Gate" and "Short Gate" in Figure 4.1, which were used to form a tail/total PSD metric:

$$PSD = \frac{Q_{tail}}{Q_{total}}, \tag{4.1}$$

where, $Q_{tail} = Q_{long} - Q_{short}$ and $Q_{total} \equiv Q_{long}$. This is shown in Fig 4.2 which is a plot of PSD versus pulse integral. Neutron pulses, having proportionally more delayed light than

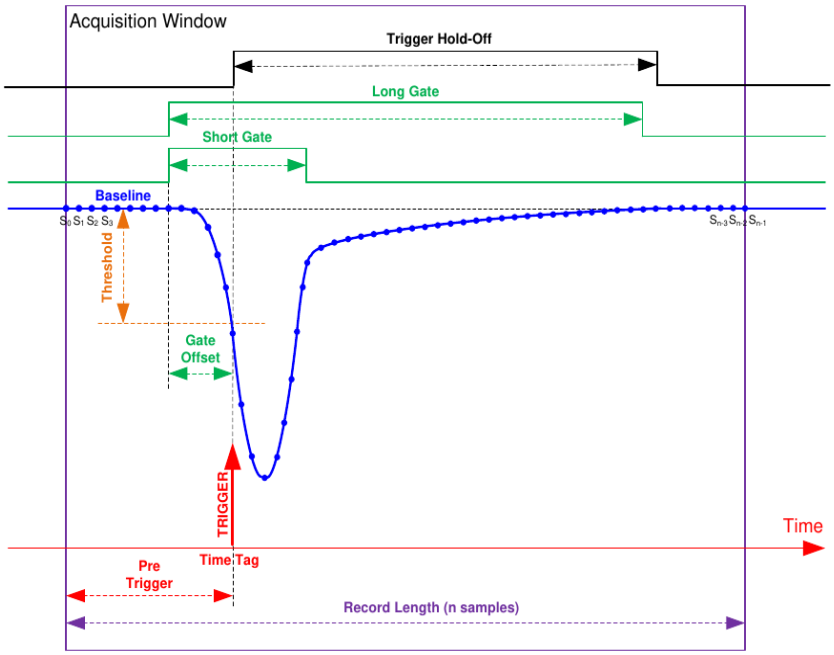

Figure 4.1: Diagram of DAQ parameters and record settings. Image reproduced from [16]

equivalent energy γ-ray pulses, have a larger value of PSD and correspond to the top band in the figure. γ-ray pulses correspond to the lower band.

4.3 Timing Calibrations

Incident neutron energy was determined using a Time-of-Flight (TOF) technique. Frame overlap necessitates a relative instead of absolute timing scheme. For each event, a "time-since-last-*rf*" was calculated. It is given by

$$\Delta t_{event} = t_{rf} - t_{event}, \tag{4.2}$$

where, t_{event} is the scintillator timestamp and t_{rf} is the cyclotron rf timestamp. Neutron events are converted from "time since-last-*rf*" space to TOF space by adding a calibration constant that represents the difference between the γ-ray TOF and the measured Δt_γ. The γ-ray flash peak had a temporal width of 8.5 ns sigma for the 4.4 m data set (6.0 ns sigma for the 9.4 m data set) and represents our timing resolution. The neutron TOF is given by,

$$TOF_n = \Delta t_n - \Delta t_\gamma + L/c, \tag{4.3}$$

where TOF_n is the neutron TOF, Δt_γ is the measured γ-ray time relative to the rf and L/c is the γ-ray TOF. The neutron energy (E_n) is then inferred from the TOF,

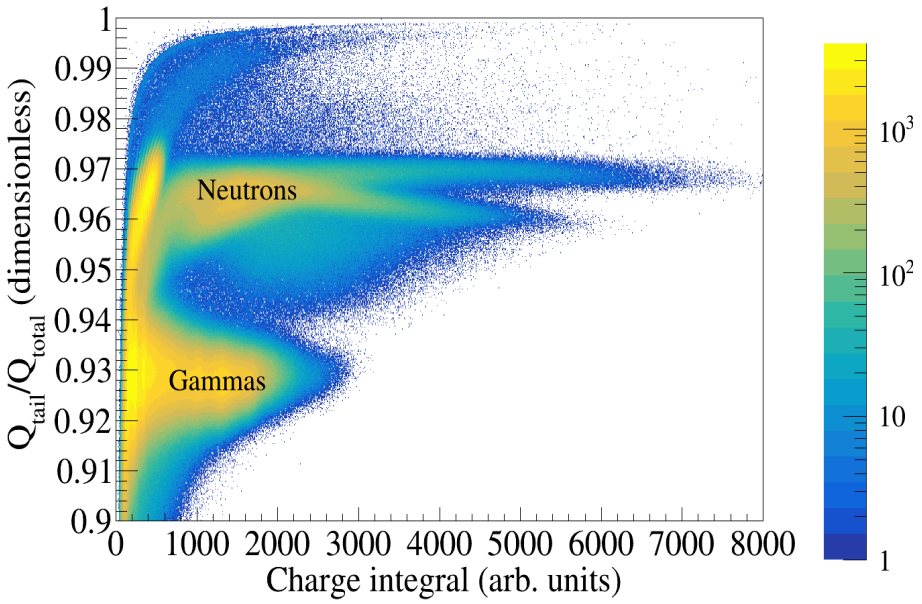

Figure 4.2: CLYC PSD plot.

$$E_n = (\gamma - 1)mc^2 \left(\frac{1}{\sqrt{1 - \frac{d^2}{TOF^2 c^2}}} - 1 \right) mc^2 \tag{4.4}$$

where, γ is the Lorentz Factor and d is the flight path length. Figure 4.3 is a plot of γ-ray counts versus Δt for an example data file. The strong peak at 80 ns is the γ-ray flash. The DAQ observes a time signal for the γ-ray at time Δt_γ. However, the true arrival time was TOF_γ (equal to L/c). The difference between the recorded and true arrival times is the time calibration (TOF_{cal}) where $TOF_{cal} = L/c - \Delta t_\gamma$.

Time trigger walk, as a result of leading edge triggering, was observed for events with small charge integral values. Figure 4.4 shows γ-ray gated raw CLYC data for both path lengths. The vertical band is the γ-ray flash. The γ-ray band in the 9.4 m data set appears as two peaks due to timing shifts throughout the experiment. This was corrected for by the timing calibration. For events with small light yield values (4 a.u. for 4.4 m; 1 a.u. for 9.4 m) the γ-ray band is not vertical but slopes to higher times. Over the range of interest, the time-of-flight was seen to walk by 1 ns, resulting in a neutron energy walk of roughly 1%.

The different pulse shapes between neutron and γ-ray events can produce another type of timing error resulting from their differing rise times. This effect was recently reported by [48] who observed a time bias values of 2-4 ns when using a constant fraction discrimination

Parameter	CLYC-4.4 m	CLYC-9.4 m	Cyclotron *rf*
Channel	2	2	7
Record Length	1472 ns	1472 ns	1472 ns
Pre-Trigger	288 ns	288 ns	288 ns
Polarity	Negative	Negative	Negative
Fixed Baseline	15280	15280	0
DC Offset	8 %	8 %	8%
Input Dynamic Range	2 Vpp	2 Vpp	2 Vpp
Mode	Leading Edge	Leading Edge	Leading Edge
Threshold	300 LSB	250 LSB	100 LSB
Trigger Hold-Off	8496 ns	8496 ns	192 ns
Input Smoothing	16 samples	16 Samples	16 samples
Energy Coarse Gain	160 fC/LSB/Vpp	640 fC/LSB/Vpp	40 fC/LSB/Vpp
Gate	8000 ns	8000 ns	300 ns
Short Gate	148 ns	148 ns	124 ns
Pre-Gate	108 ns	108 ns	88 ns

Table 4.1: Summary of DAQ Settings.

(CFD) setup. We investigated this potential timing bias by calculating the time trigger offset between γ-ray and neutron pulses for our leading edge discrimination setup. For all pulse heights and reaction channels used in this work, it was observed to be negligible.

4.4 Monte Carlo Modeling

The detector response was simulated using the GEANT4 software package [2] to guide interpretation of the experimental data. A one inch by one inch, square, parallel, uniform source from 0.5 - 14 MeV was directed to the side of the scintillator crystal. The simulations were performed at two distances: 4 m and 9 m. Neutrons incident on CLYC can undergo many reactions, each of which, produces a characteristic kinematic band. The amount of scintillation light produced for a given reaction is a function of the neutron energy, the reaction Q-value,

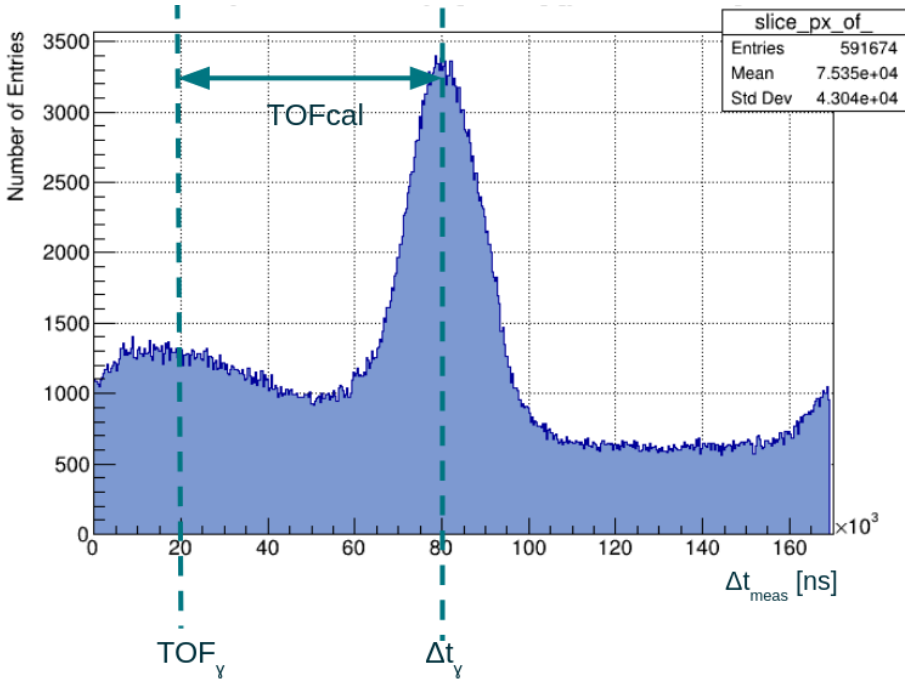

Figure 4.3: Timing Calibration. TOF_{cal} is the between the true γ-ray TOF (TOF_γ) and the DAQ timestamp (Δ t_γ).

and the reaction product particle type. The light output vs. neutron energy results for the 9 m model are shown in Fig. 4.5. A number of things are apparent. First, the energetic ^{6}Li(n,α)t reaction, ($Q_{n,\alpha}$ = 4783 keV), produces a well separated band with a large light yield. Second, the smaller Q-value reaction ^{35}Cl(n,p_0), ($Q_{n,p}$ = 615 keV), produces a bright band at a lower light yield. Third, ^{35}Cl(n,pγ) bands are significant and appear below the (n,p_0) band. Fourth, all other other reactions including those on ^{37}Cl and ^{7}Li tend to lie on top of one another below the (n,p_0) band. This also implies that calculation of ^{35}Cl(n,pγ) and ^{35}Cl(n,α) cross sections may be not be possible. Lastly, a significant amount of downscatter is seen in the ^{6}Li(n,α)t reaction. The downscatter represents a fairly uniform background at light yields below the unscattered ^{6}Li(n,α)t band and continues until it reaches the ^{6}Li(n,α)t Q-value.

In the experimental case, these bands do not simply continue uninterrupted to arbitrarily long TOF as shown in Fig. 4.5, but instead will "wrap" over the previous data at some point. This "wrap point" is dependent on the flight path length. Fig. 4.6 and 4.7 show the GEANT4 simulations in which the output has been wrapped for two different path lengths. For a path length of 8.5 m, the wrap point occurs at an energy of 3 MeV and for a 4 m path length it occurs at 1.2 MeV. Thus, by utilizing two different path lengths the unwrapped energy range is maximized. Due to space constraints within the cave the experimental detector locations

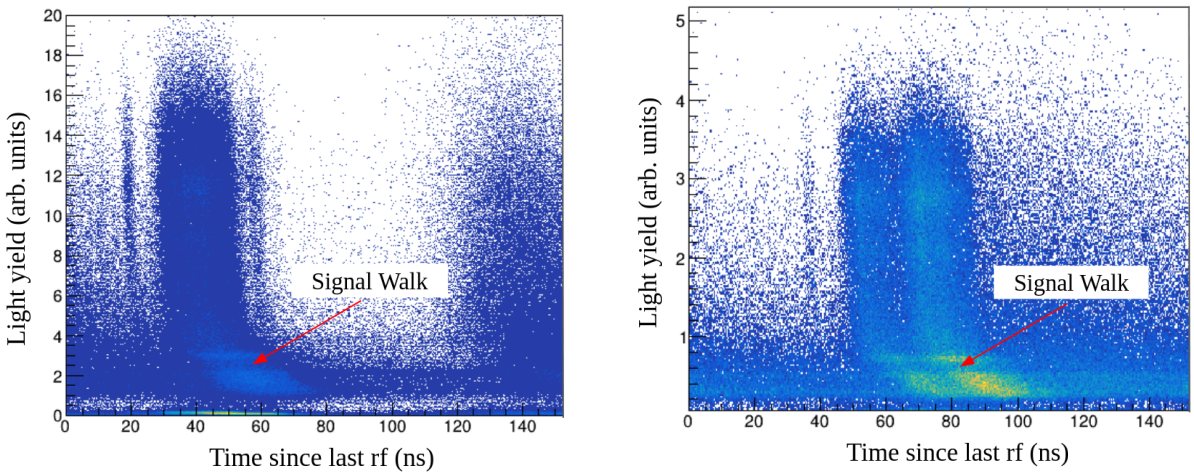

(a) 4.4 m (b) 9.4 m

Figure 4.4: Gamma-ray gated raw CLYC spectra. The change in the γ-ray peak centroid at low light yield is due to signal walk.

were 9.4 m and 4.4 m.

4.5 ^{35}Cl(n,p$_0$)

Fig. 4.8 and Fig. 4.9 show the experimental integrated charge vs. time-of-flight data for path lengths of 4.4 m and 9.4 m respectively. For clarity, two frames are shown. Viewed in this way, the kinematic bands can be seen to continue from one frame to the next. This is equivalent to the picture in which a band exits the figure on the right side and then reappears on the left side. The experimental band structure is similar to that seen in the GEANT4 model with the addition of experimental resolution. The zeroth frame of the energetic ^{6}Li(n,α)t band is at the top of the figure. Subsequent frames are hidden by the emergence of lower Q-value reactions but it eventually reappears as a horizontal band. This represents the minimum possible light yield from the reaction and is largely due to the 240 keV resonance but also contains all lower energy events. A 240 keV neutron has a TOF of 650 ns for a 4.4 m flight path (1387 ns for 9.4 m) which corresponds to 3.8 *rf* periods. As can be seen from the model in Fig.4.6, the band is nearly flat after just two wraps. Thus, by the time the band has reached 240 keV it is, within the resolution of the detector, perfectly flat. This band, which includes events down to thermal energies (comprised of almost 12,000 wraps) is considered perfectly time independent. The ^{6}Li(n,α)t band is unique in that it produces two light-producing particles which are emitted back-to-back in the CoM frame. They have the following kinematic relationship

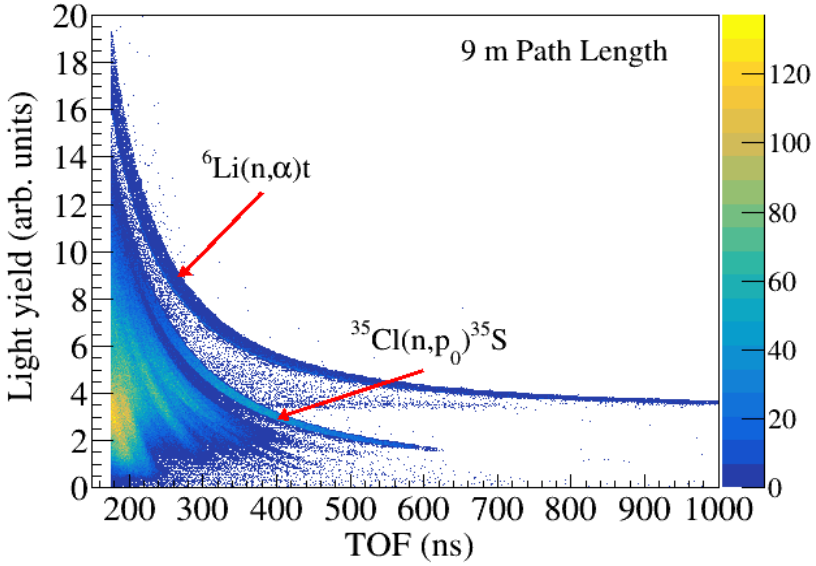

Figure 4.5: GEANT4 simulation showing the various kinematic bands. The desired ^{6}Li(n,α)t and ^{35}Cl(n,p$_0$) bands are bright and well separated.

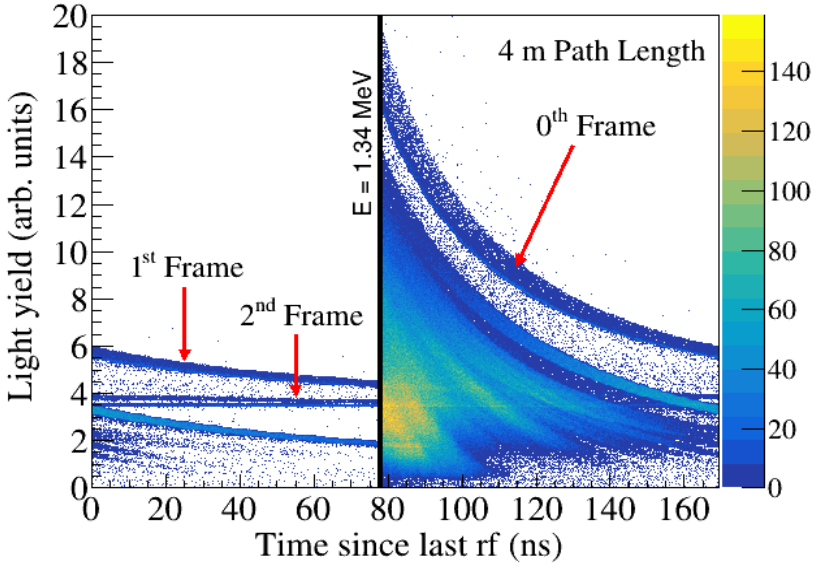

Figure 4.6: Wrapped GEANT4 simulation for a path length of 4 m with a wrap point at 1.34 MeV.

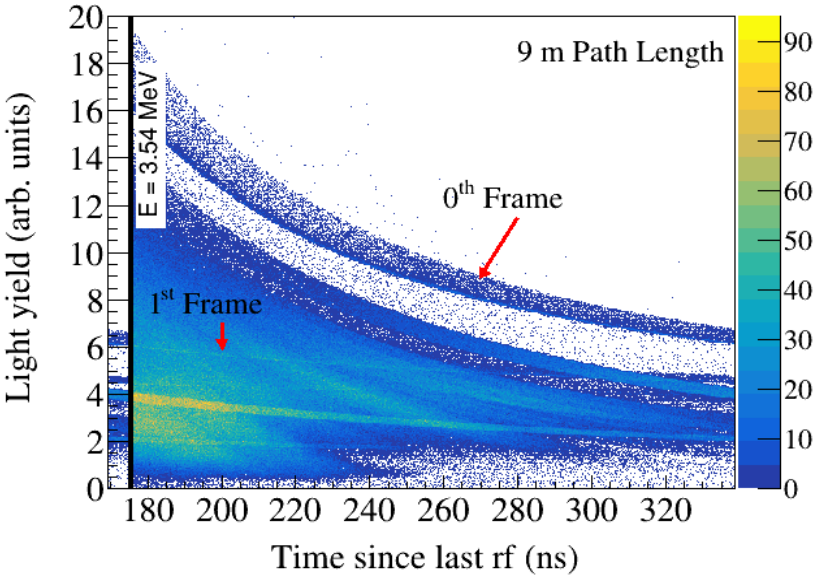

Figure 4.7: Wrapped GEANT4 simulation for a path length of 9 m with a wrap point at 3.54 MeV.

$$T_\alpha = \frac{Q}{1 + m_\alpha/m_t}, \tag{4.5}$$

where, T_α is the α-particle kinetic energy, m_α and m_t are the particle masses, and Q is the reaction Q-value. The kinetic energy for the alpha is thus $(3/7)Q$ while for the triton it is $(4/7)Q$. The α-particle, having twice the nuclear charge of the triton, will be more quenched since quenching is roughly proportional to dE/dx [36]. The particles are emitted isotropically in the CoM and the exact energy sharing depends on the emission angle with respect to the CoM direction. These effects create a ^{6}Li(n,α)t band that has as a broad bi-modal distribution which is more pronounced at higher incident neutron energies (short TOF). Conversely, the ^{35}Cl(n,p$_0$) band, which has only one light producing particle appears as a single, narrow band and is located beneath the Li band due to its lower Q-value.

The determination of the ^{35}Cl(n,p$_0$) in this work is done through a ratio method. The cross section is determined using the ^{6}Li(n,α) cross section via

$$\sigma^{Cl}(E) = \frac{0.95}{6 \cdot 0.76} \frac{R^{Cl}(E)}{R^{Li}(E)} \sigma^{Li}(E), \tag{4.6}$$

where, R^{Cl} and R^{Li} are the number of observed ^{35}Cl(n,p$_0$) and ^{6}Li(n,α)t reactions for a given incident neutron energy. The constants account for isotopic and chemical abundances of ^{6}Li and ^{35}Cl.

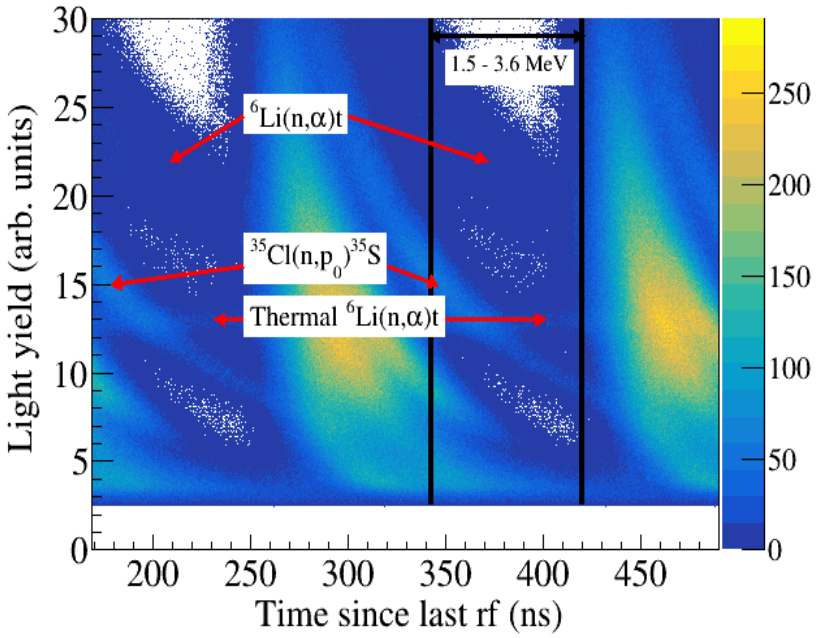

Figure 4.8: Various kinematic reaction bands for a path length of 4.4 m

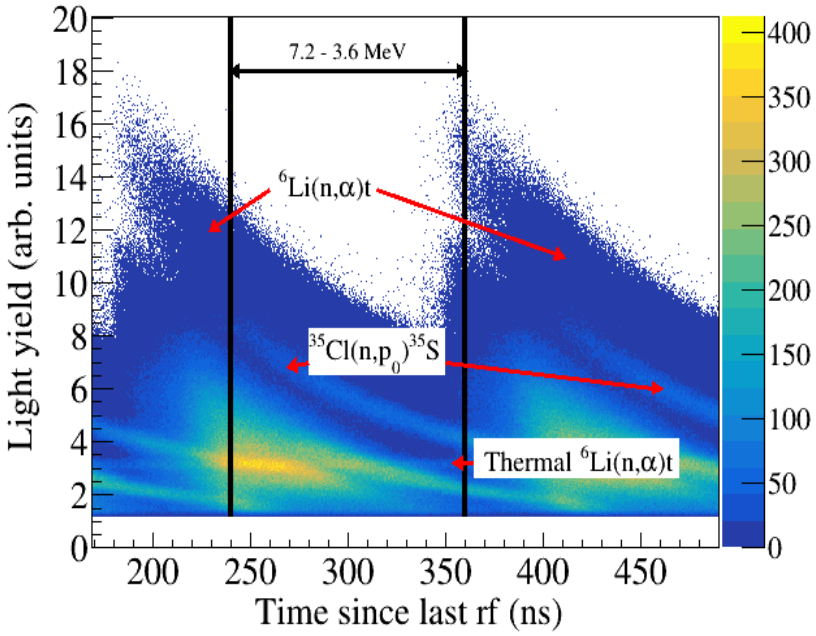

Figure 4.9: Various kinematic reaction bands for a path length of 9.4 m

The observation of the ratio requires that the bands from both reactions yield reliable estimated counts. This leads to discontinuous limited regions over which the cross section can be ascertained in this work. The accessible regions for the two flight paths are 2.02-3.49 MeV for the short flight path and 3.91-7.46 MeV for the 9.4 m long flight path. The upper limit of the long flight path is due to a lack of statistics, while the upper bound for the shorter flight path is due to clipping of the QDC. In both cases frame overlap provides a limit on the lower energy.

The accessible region was divided into ten equally sized TOF projections, this number being determined by the time resolution. For each TOF projection, a fitting model consisting of twenty-one parameters (with three fixed) was applied. The model consisted of a single Gaussian for the unwrapped ^{35}Cl(n,p$_0$) band, a sum of two Gaussians for the unwrapped ^{6}Li(n,α)t band, and an empirical background consisting of three Gaussians and a polynomial. Two Gaussians were used for the unwrapped ^{6}Li(n,α)t band due to the energy sharing between the α and triton reaction products as discussed above. The background model consisted of one Gaussian for the singly wrapped Li band, a second Gaussian for the time-independent highly-wrapped Li band, a third Gaussian to capture all other reactions (i.e. low light-producing reactions such as the ^{35}Cl(n,α) and ^{35}Cl(n,p$_i\gamma$) and ^{37}Cl(n,x) reactions, as well as wrapped ^{35}Cl(n,p$_0$) bands and a second order polynomial to capture downscatter effects.

For each TOF projection, a χ^2 minimization was performed against this model to determine the relative reaction rates of ^{35}Cl(n,p$_0$) with respect to ^{6}Li(n,α)t using the Minuit2 package provided by the ROOT data analysis framework [11]. This minimization was used to obtain parameter estimates as well as uncertainties.

Since the highly wrapped Li band is time-independent, its parameters are first determined by examining regions where little else is present (i.e. 420 ns for 4.4 m and 360 ns for 9.4 m), and then fixing the parameters during the χ^2 minimization. For the Gaussian consisting of "other" reactions, only the high energy tail is used as these reactions always occur at a light yield below that of the reactions of interest. Four representative results from each data set are shown in Figs. 4.10 - 4.17. In these figures it can be seen that as the projections sweep through TOF space, the locations and relative heights of the reaction bands change.

Fig. 4.18 shows the results using using equation 4.6. The data is seen to be consistent within error with Kuvin *et al.* [39] over the measured energy range.

4.6 Uncertainty Quantification

When calculating the cross section in ratio to a well known reference reaction, sources of uncertainty such as those in the flux, solid angle, detector efficiency, deadtime, and downscatter effects cancel out. This leaves the flight path length and the ^{6}Li(n,α)t cross section

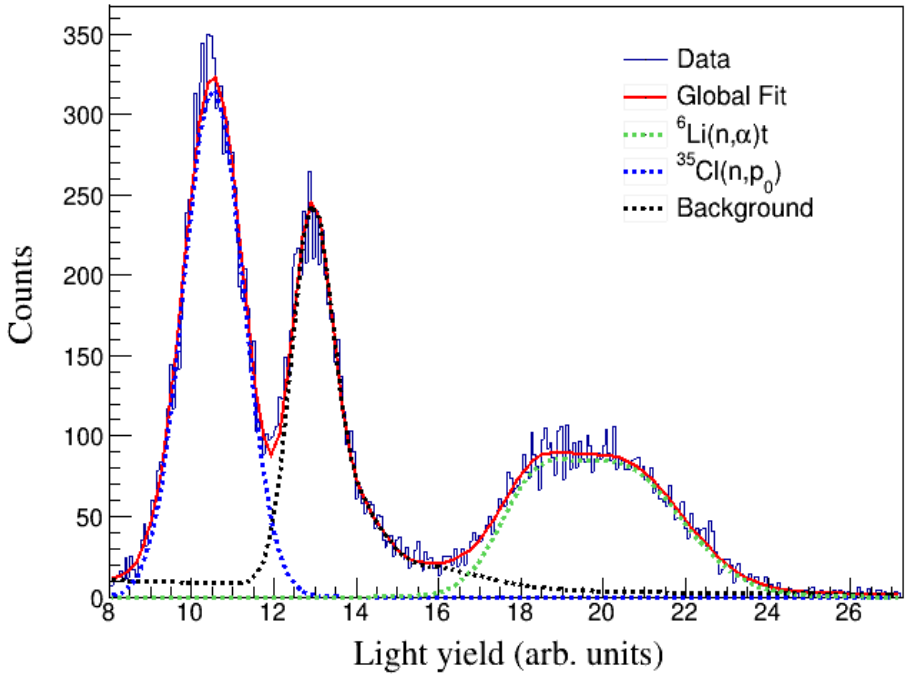

Figure 4.10: Representative fit of 4.4 m data set for a neutron energy of 2.02 MeV.

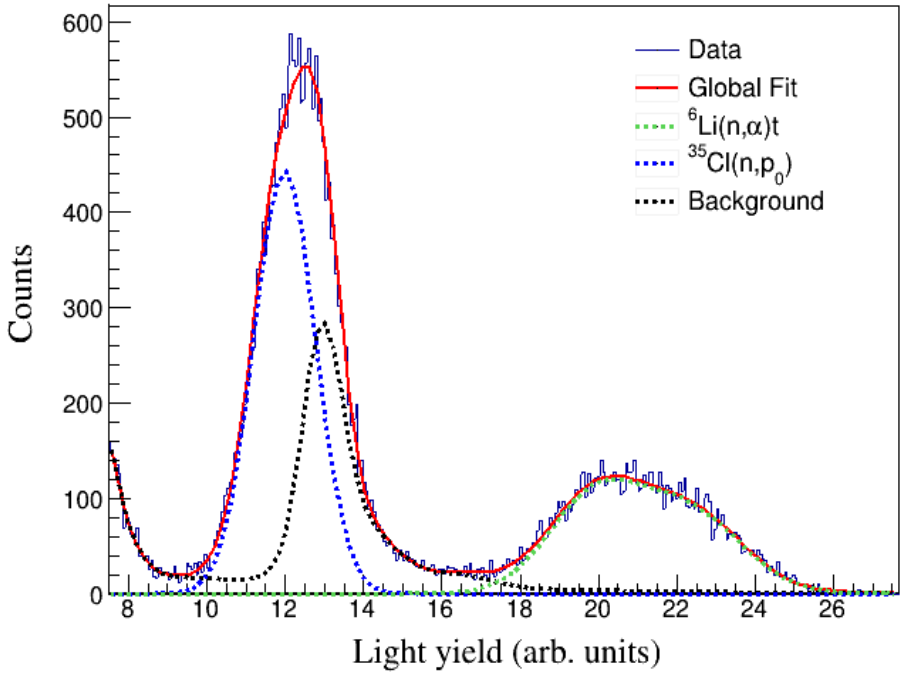

Figure 4.11: Representative fit of 4.4 m data set for a neutron energy of 2.39 MeV.

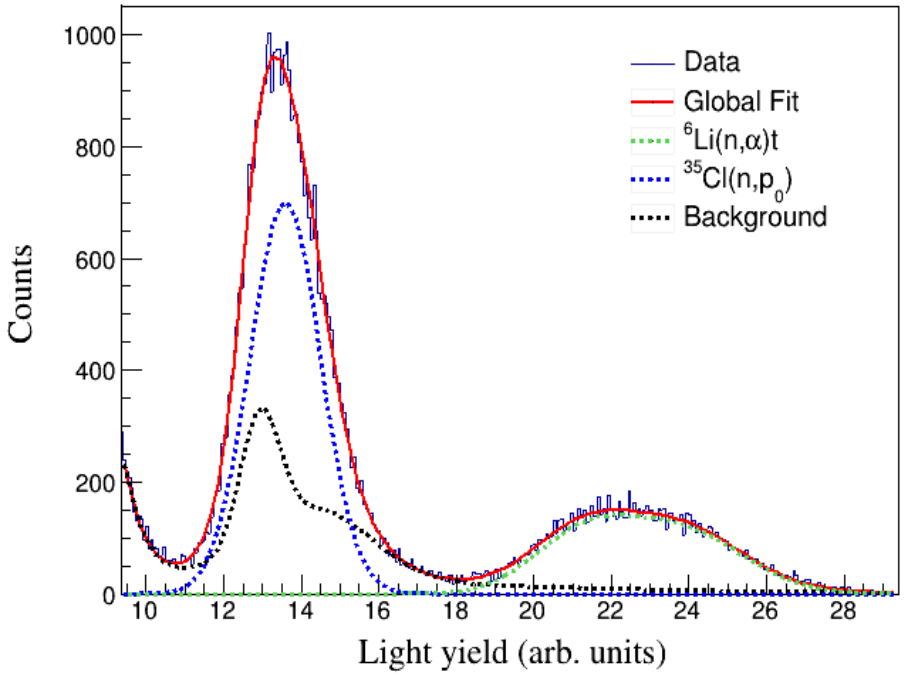

Figure 4.12: Representative fit of 4.4 m data set for a neutron energy of 2.86 MeV.

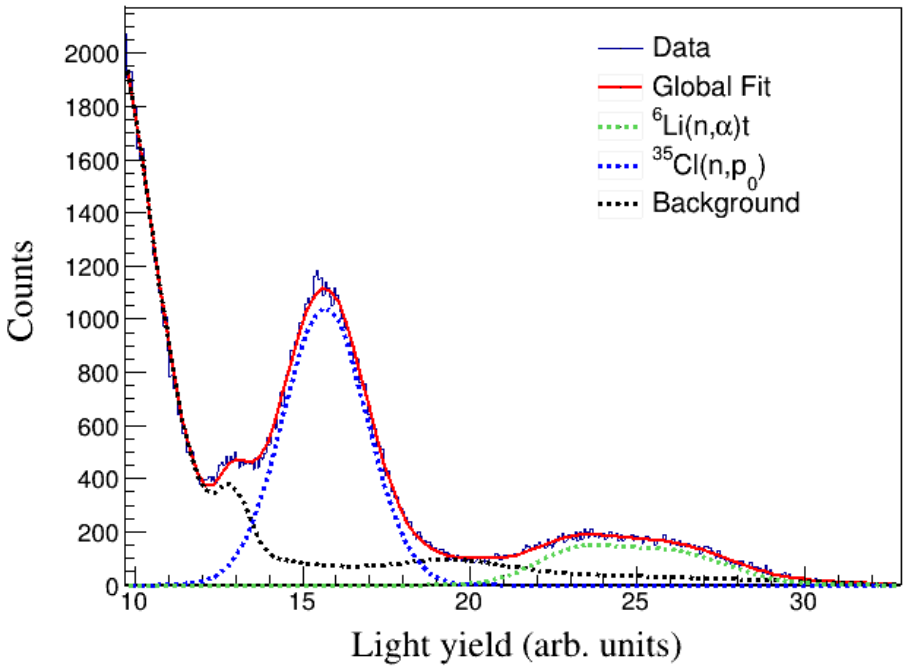

Figure 4.13: Representative fit of 4.4 m data set for a neutron energy of 3.49 MeV.

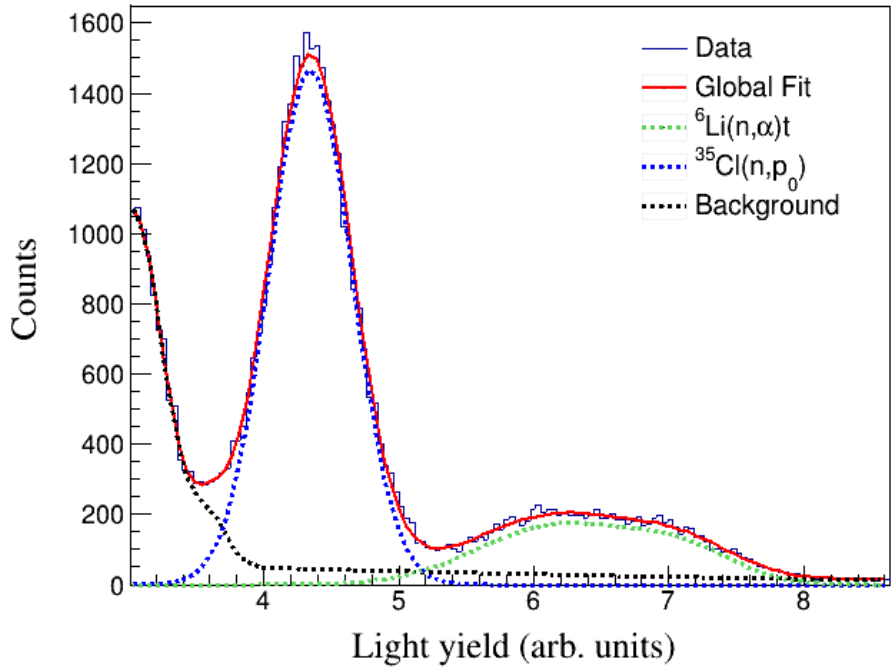

Figure 4.14: Representative fit of 9.4 m data set for a neutron energy of 3.91 MeV.

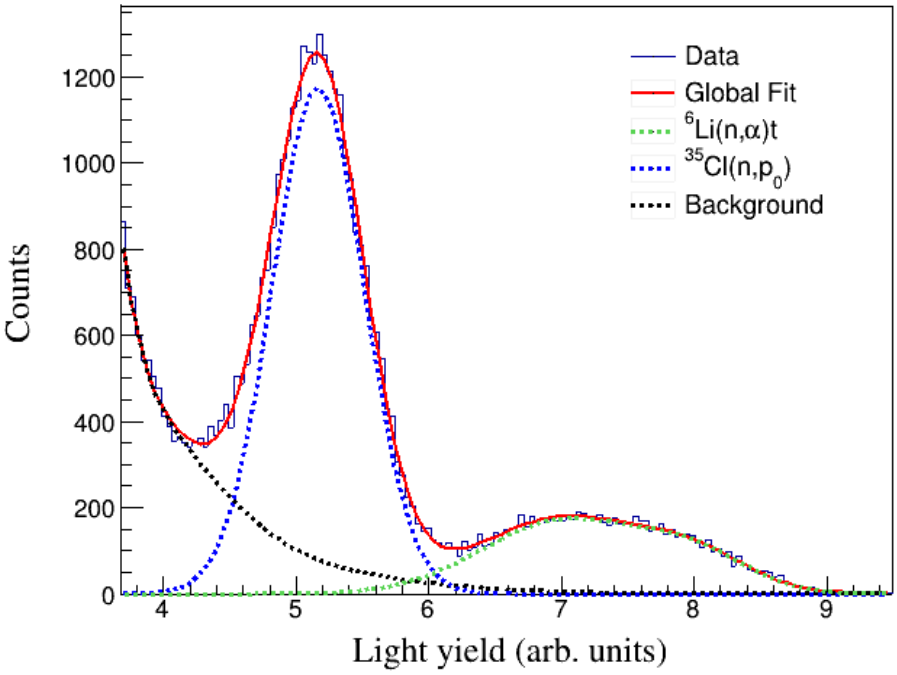

Figure 4.15: Representative fit of 9.4 m data set for a neutron energy of 4.74 MeV.

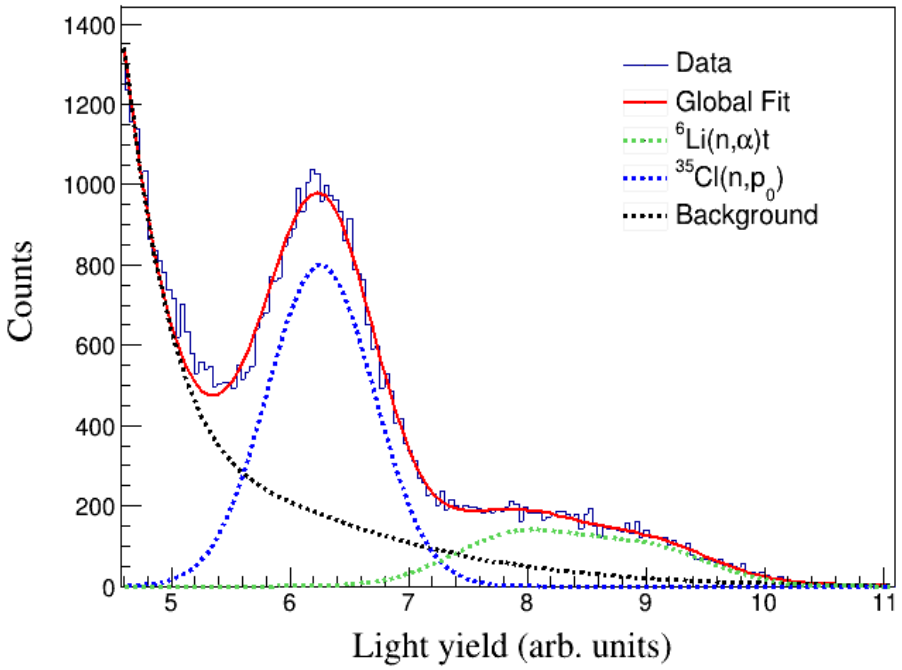

Figure 4.16: Representative fit of 9.4 m data set for a neutron energy of 5.87 MeV.

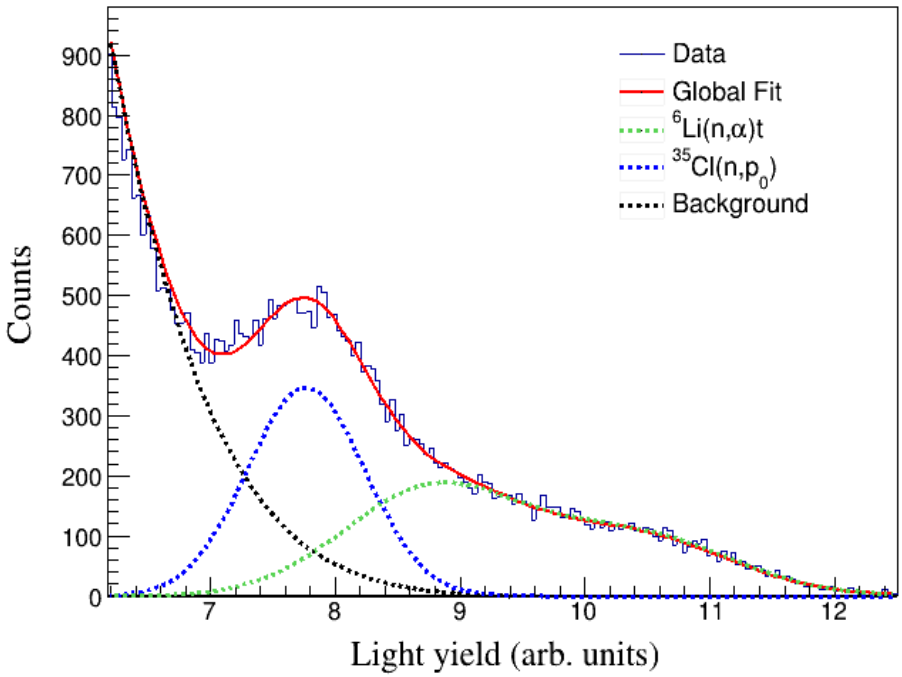

Figure 4.17: Representative fit of 9.4 m data set for a neutron energy of 7.46 MeV.

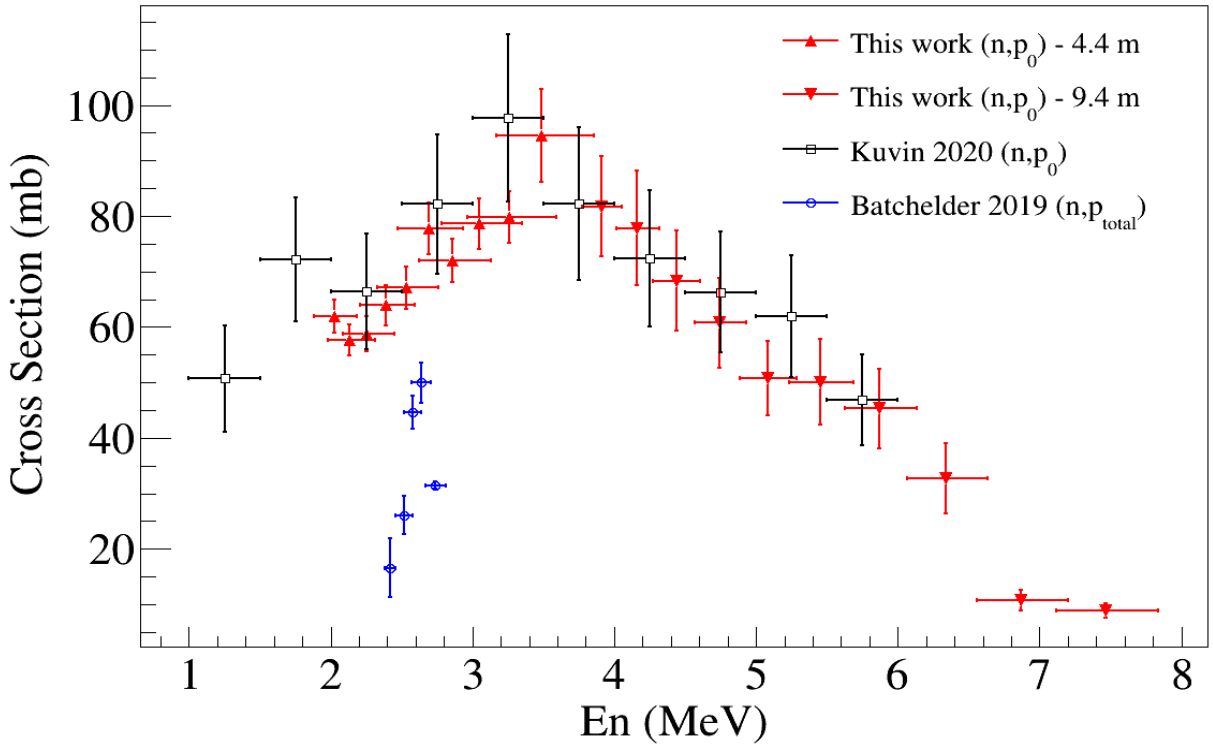

Figure 4.18: Measured energy differential ^{35}Cl(n,p$_0$) cross section. The data is seen to be consistent within error with Kuvin *et al.* over the measured energy range.

as the only significant sources of systematic uncertainty. Unfortunately, their impact on the calculated cross section is complicated due to effects on the timing calibration, neutron energy, value of reference cross section, etc. Thus, a Monte Carlo approach was chosen to estimate these uncertainties. An additional potential complication is the presence of energy-dependent ^{6}Li(n,α)t correlations. However, correlation data is not yet available for ENDF/B-VIII.1 (the evaluation used in calculating the cross section). Correlation data is available for ENDF/B-VIII.0 but only up to 4 MeV. For this reason, the uncertainties in the ^{6}Li(n,α)t were assumed to be uncorrelated.

Analytical vs. Monte Carlo Uncertainty Propagation

Traditional analytical uncertainty propagation involves the use of input variable probability distribution functions (PDFs) and analytical propagation formulas to explicitly calculate an uncertainty for a given desired final variable. For example, let C be the desired final variable and let A and B be, possibly correlated, inputs with uncertainties σ_A and σ_A. Let C be some function of A and B, $C = f(A, B)$. The uncertainty in C, σ_C, is given by the following formula [57],

E_n (MeV)	σ (mb)	E_n (MeV)	σ (mb)
$2.02 \pm^{0.16}_{0.14}$	61.95 ± 3.11	$3.91 \pm^{0.14}_{0.13}$	81.77 ± 9.14
$2.14 \pm^{0.17}_{0.16}$	57.62 ± 2.85	$4.16 \pm^{0.15}_{0.15}$	77.85 ± 10.33
$2.26 \pm^{0.19}_{0.17}$	58.75 ± 3.15	$4.44 \pm^{0.17}_{0.16}$	68.32 ± 9.06
$2.39 \pm^{0.21}_{0.18}$	63.92 ± 3.71	$4.74 \pm^{0.19}_{0.18}$	60.76 ± 8.06
$2.53 \pm^{0.23}_{0.20}$	67.07 ± 3.85	$5.08 \pm^{0.21}_{0.20}$	50.82 ± 6.74
$2.69 \pm^{0.25}_{0.22}$	77.76 ± 4.71	$5.45 \pm^{0.23}_{0.22}$	50.06 ± 7.76
$2.86 \pm^{0.27}_{0.24}$	71.93 ± 3.98	$5.87 \pm^{0.26}_{0.24}$	45.29 ± 7.24
$3.05 \pm^{0.30}_{0.26}$	78.64 ± 4.57	$6.34 \pm^{0.29}_{0.27}$	32.70 ± 6.33
$3.26 \pm^{0.33}_{0.29}$	79.79 ± 4.75	$6.87 \pm^{0.33}_{0.31}$	10.72 ± 1.80
$3.49 \pm^{0.37}_{0.32}$	94.48 ± 8.38	$7.46 \pm^{0.38}_{0.35}$	8.94 ± 1.30

Table 4.2: Angle-integrated ^{35}Cl(n,p$_0$) cross section data

$$\sigma_C^2 = \left(\frac{\partial f}{\partial A}\sigma_A\right)^2 + \left(\frac{\partial f}{\partial B}\sigma_B\right)^2 + 2\frac{\partial f}{\partial A}\frac{\partial f}{\partial b}\sigma_{A,B}. \tag{4.7}$$

This approach works well for simple functions in which the partial derivatives can be easily calculated. For the case of the $^{35}\mathrm{Cl}(n,p_0)^{35}\mathrm{S}$ calculation described here, it would be very difficult.

Modern computing speeds have allowed a new method, the Monte Carlo approach, to be used for difficult technical problems. Monte Carlo uncertainty estimation is a stochastic process which involves random sampling of known PDFs and uses these results to produce a data set for the desired variable. Statistical information for the variable is then extracted from this data set. Continuing with the example above, σ_C is determined in the following manner. For each uncorrelated inputs A and B, generate a PDF centered around zero with the correct standard deviation. Then, randomly sample the PDFs n times to obtain values r_A^i and r_B^i, where i represents the i^{th} sampling. Add this to the mean of the PDF, $A^i = \bar{A} + r_A^i$. The i^{th} value for the desired variable C is then,

$$C^i = f(\bar{A} + r_A^i, \bar{B} + r_B^i).$$

The mean, $\bar{C}$ and standard deviation σ_C for the set of n C^i values is then calculated.

^{35}Cl$(n, p_0)^{35}$S Monte Carlo routine

Analysis parameters with inherent uncertainty in this work include the flight path length and the ^{6}Li(n, α)t cross section. Their impact on the calculated cross section is complicated due to highly correlated effects on the timing calibration, neutron energy, value of reference cross section, etc. Propagation of these uncertainties was performed via Monte Carlo, where we follow the approach given by [54]. The flight path length was randomly sampled 1,000 times from a Gaussian distribution with the standard deviation set at 1 cm. For each trial, the uncertainty in the ^{6}Li(n, α)t cross section was incorporated by multiplying the cross section uncertainty with a random number sampled from a Gaussian with a standard deviation of one. This was then added to energy window averaged cross section. Uncorrelated ^{6}Li(n, α)t uncertainties from ENDF/B-VIII.0 were used since covariance data is not available for ENDF/B-VIII.1. For each trial, a χ^2 minimization using the MIDGRAD algorithm in the Minuit2 minimization package provided by ROOT [11], was performed to determine the model parameter estimates and the ^{35}Cl(n, p_0) cross section computed. The χ^2 was used to weight the trial solutions as described by Birge [7]. Thus, the weighted mean of the 1,000 trial solutions is given by,

$$\bar{\sigma^j} = \frac{\sum_{i=1}^{N} w_i^j \sigma_i^j}{\sum_{i=1}^{N} w_i^j} \tag{4.8}$$

where, $\bar{\sigma^j}$ weighted mean of the 1,000 trial solutions for TOF window j, σ_i^j is the solution for trial i for TOF window j, and w_i^j is the weighting factor for trial i and TOF window j which is given by,

$$w_i = \frac{1}{\sqrt{\chi_i^2}}. \tag{4.9}$$

The reported cross section is the mean of this distribution. The uncertainty was determined via the standard deviation of the above distribution plus the quadrature added uncertainties from the Li and Cl abundances. The enrichment of ^{6}Li was assumed to be 95±1% and the isotopic abundance of ^{35}Cl is 0.7576±0.001. This above distribution was also used to construct the weighted covariance matrix as given by,

$$cov_{\sigma^j,\sigma^k} = \frac{\sum_{i=1}^{N} w_i^j w_i^k (\sigma_i^j - \bar{\sigma^j})(\sigma_i^k - \bar{\sigma^k})}{\sum_{i=1}^{N} w_i^j w_i^k}. \tag{4.10}$$

69.63	1.29	0.85	-1.31	-1.05	-0.54	0.37	0.43	-1.22	-0.66
1.29	22.08	0.56	0.00	0.13	-0.46	0.49	0.10	-0.15	0.52
0.85	0.56	20.45	-0.03	0.75	0.08	-0.06	-0.15	0.45	0.08
-1.31	0.00	-0.03	15.49	0.22	0.31	-0.15	0.53	0.22	-0.42
-1.05	0.13	0.75	0.22	21.78	-0.99	-1.02	-0.17	-0.52	-0.87
-0.54	-0.46	0.08	0.31	-0.99	14.52	-0.20	0.19	0.39	-0.28
0.37	0.49	-0.06	-0.15	-1.02	-0.20	13.49	0.53	-0.34	0.13
0.43	0.10	-0.15	0.53	-0.17	0.19	0.53	9.67	0.75	0.08
-1.22	-0.15	0.45	0.22	-0.52	0.39	-0.34	0.75	7.89	0.34
-0.66	0.52	0.08	-0.42	-0.87	-0.28	0.13	0.08	0.34	9.37

Table 4.3: Covariance Matrix: 4.4 m data set

Table 4.3 is the covariance matrix for the 4.4 m data set and Table 4.4 is the covariance matrix for the 9.4 m data set.

1.68	-0.13	0.24	0.60	0.16	-0.24	0.34	-0.56	0.66	-0.15
-0.13	3.23	-0.36	-0.84	1.03	0.45	-0.13	-0.29	-1.33	-0.17
0.24	-0.36	39.95	1.33	3.14	-1.29	2.61	2.76	-1.22	1.67
0.60	-0.84	1.33	52.30	-1.15	1.12	2.83	1.48	2.29	-2.52
0.16	1.03	3.14	-1.15	60.07	2.59	-0.87	1.94	-2.02	-1.69
-0.24	0.45	-1.29	1.12	2.59	45.21	3.72	-2.11	2.26	-1.89
0.34	-0.13	2.61	2.83	-0.87	3.72	64.71	3.01	0.96	-1.59
-0.56	-0.29	2.76	1.48	1.94	-2.11	3.01	81.76	3.08	-0.35
0.66	-1.33	-1.22	2.29	-2.02	2.26	0.96	3.08	106.20	-0.40
-0.15	-0.17	1.67	-2.52	-1.69	-1.89	-1.59	-0.35	-0.40	83.01

Table 4.4: Covariance Matrix: 9.4 m data set

Chapter 5

GENESIS Analysis and Results

5.1 Experimental Setup

The Gamma Energy Neutron Energy Spectrometer for Inelastic Scattering (GENESIS) is an array of gamma and neutron detectors designed to measure neutron inelastic cross section using n-γ coincidences. Twenty-six EJ-309 liquid scintillator detectors (only used for timing in this work) which are arranged a quarter shell and perpendicular to the beam direction are used for neutron detection. Gamma-rays are detected with two Eurisys 2-fold segmented N-type HPGe CLOVER detectors, equipped with BGO anti-Compton shields, two Ortec Pop-Top HPGe detectors (not used in this work), and a LaBr inorganic scintillator detector (not used in this work). The γ-ray detectors are located in a plane at beam height surrounding the center of the array. For this work the CLOVER detectors were placed at 86° and 42° relative the beam direction. Figure 5.1 shows a view of GENESIS looking upstream towards the vault.

The experiment was conducted in August, 2021 over five days. Prior to the start of the experiment, the beam profile was measured to maximize beam on target. The beam profile measurement system consists of a 1" liquid scintillator can move in the plane transverse to the beam direction. By monitoring the count rate in the scintillator and varying the beam location the point of maximum beam intensity, beam size and shape, were determined.

The 10.4228±0.0001 g NaCl target was made by pressing reagent grade NaCl (Sigma-Aldrich - lot number: BCBQ6633V) in a desktop pellet press (Across International) with a 50 mm diameter die. The mass was measured using a Mettler Toledo AL204 precision scale. The completed target was double bagged and hung at an angle from the target holder. Hanging the bag at an angle ensures that the target does not shift inside the bag. The target holder consisted of an aluminum and steel U-shaped frame and the whole apparatus was placed at 45° relative to the beamline to minimize the amount of target material through which reaction products must travel in order to reach a detector. The target was centered

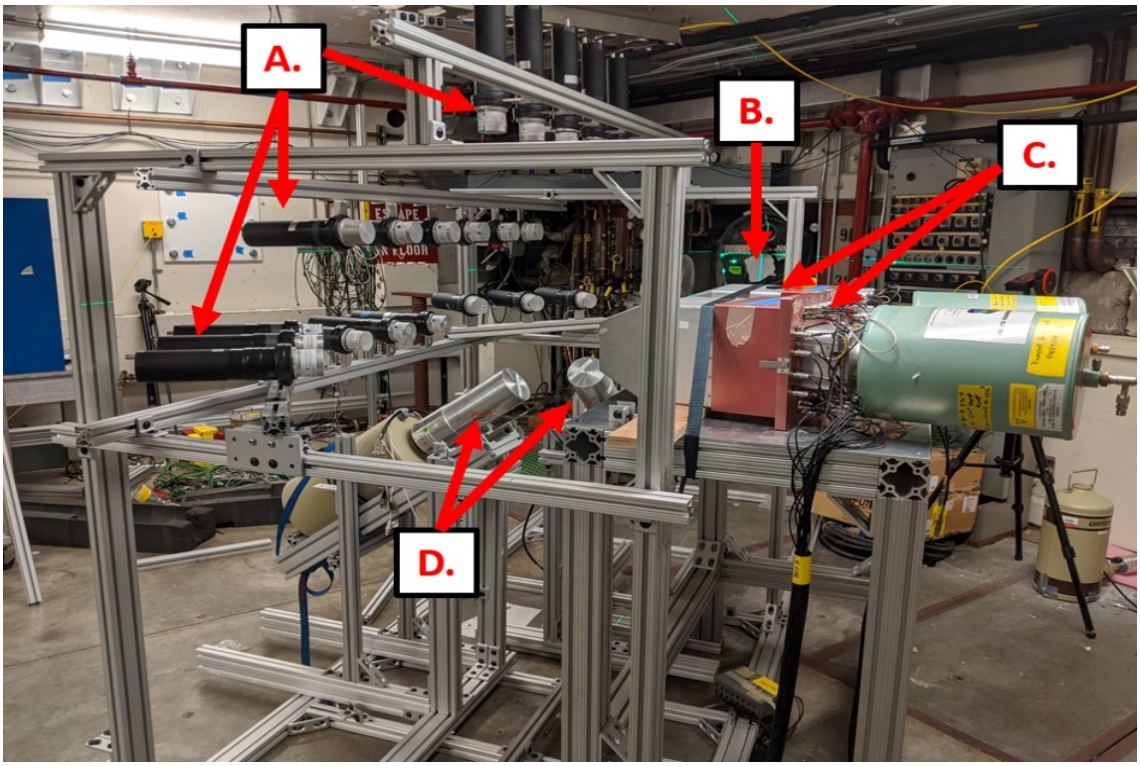

Figure 5.1: The GENESIS Array. A: EJ-309 organic liquid scintillators. B: Beam pipe. C: CLOVER detectors with BGO Compton suppression and Heavy-met shields. D: Ortec Pop-Top HPGes. Figure courtesy Joseph Gordon.

in the beam by aligning a Huepar 902CG cross line laser level with predetermined beamline reference points on the cave walls. Once the target was hung, its position was measured using a Leica Disto S910 laser distance meter.

Data acquisition

Data acquisition was performed by three Mesytec MDPP-16 digitizer boards [51]. EJ-309 signals were received by two of the boards using the Mesytec QDC firmware while the clover and BGOs signals were received by the third board running the Mesytec SCP firmware. Each QDC event contains a short integral, long integral, and timestamp. SCP events contain the pulse amplitude and timestamp. A trigger signal from any channel on any board is passed through a Lecroy 429 A logic fan-in/fan-out and fed back to all three boards. Additionally, each board receives a signal from the cyclotron *rf*. This allows synchronization of the detector signals with cyclotron *rf* to enable neutron TOF calculation. Detector bias voltages were provided by a 16-channel CAEN R8033DN and two 8-channel CAEN 1470ETD power supplies [26].

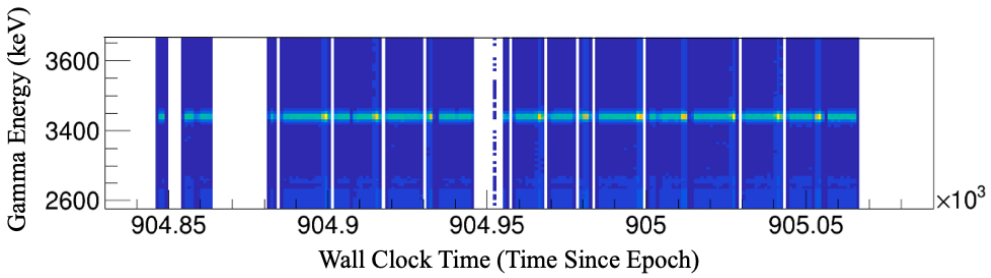

(a) Clover 4, leaf 2. No gain correction needed.

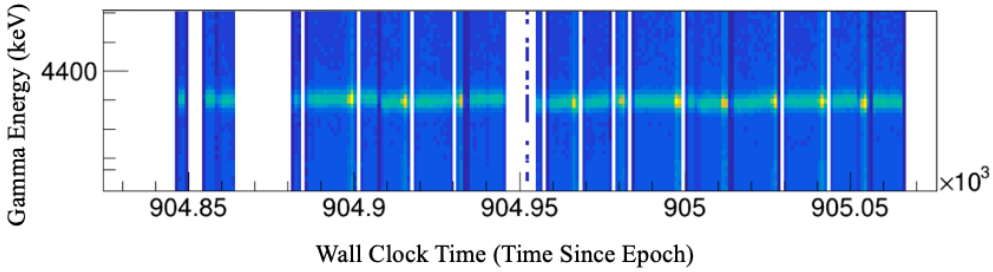

(b) Clover 3, leaf 2. Gain correction needed.

Figure 5.2: Single leaf gain drift histograms.

Energy calibration

Energy calibration was performed by placing a 0.910 μ Ci ^{152}Eu sealed source in the center of the GENESIS array. The high energy calibration ($>$ 1400 keV) was verified with using known $^{35}\mathrm{Cl}(n, n')$ lines in the beam data [13]. Detector gain was observed to drift with time in some CLOVER leaves. GENESIS post-processing software was used to provide a time-dependent gain correction. For each time bin, the gain is adjusted to match the gain at the very beginning of the run. Figure 5.2 shows examples of CLOVER leaves not requiring and requiring gain drift correction. Figure 5.2 is a 2D histogram of channel number versus wall clock time. The bright band is the 440 keV Na line. White breaks in the data indicate points when the DAQ was not running (LN fills e.g.). In this figure it is clear that the gain was stable throughout the run. This is in contrast to Figure 5.2b in which the gain is seen to vary with time.

Event timing

Each CLOVER detector is composed of four crystals, each with their own detection readout. The signals can be used independently (singles mode) or in total-detection mode, in which the energies of coincident events in separate leaves are added-back to recover the full energy of the γ-ray event. Knowledge of the relative time differences between the individual CLOVER leaves is required to establish a coincidence window for the event. A ring of BGO detectors

surrounding each CLOVER allows for Compton suppression by rejecting events in which the γ-ray Compton scatters in the CLOVER and is subsequently detected by a BGO. Again, knowledge of the relative timing, this time between the CLOVER and the BGOs is required. This was accomplished by placing a ^{252}Cf spontaneous fission source at the center of the array. The time differences between detection of the coincident fission γ-rays in a reference detector (scintillator 4) and all other detectors were accumulated and the centroids determined. From these, the relative timing between all detectors can be found [26].

Gamma-ray detection efficiency

Gamma detection efficiency was determined by placing a 0.910 μ Ci ^{152}Eu source in the center of the GENESIS array. Following add-back and Compton subtraction, each peak was fit and the efficiency calculated. The efficiency points were then fit with the following "Debertin" function from [35],

$$\epsilon(E_\gamma)^{<1400keV} = a_0 ln(E_\gamma) + a_1\frac{ln(E_\gamma)}{E_\gamma} + a_2\frac{ln(E_\gamma)^2}{E_\gamma} + a_3\frac{ln(E_\gamma)^4}{E_\gamma} + a_4\frac{ln(E_\gamma)^5}{E_\gamma}. \quad (5.1)$$

Uncertainty in the efficiency was calculated analytically from the uncertainty in the fit parameters, $a_0 - a_4$. Detection efficiency above 1400 keV was determined using a previously produced, in-house made, ^{56}Co source. The source was made by bombarding an ^{56}Fe target with protons to produce ^{56}Co via ^{56}Fe$(p,n)^{56}$Co. The same efficiency determination procedure was used as with the ^{152}Eu data except the curve was fit using the "Lin" function,

$$ln(\epsilon(E_\gamma))^{>1400keV} = a_0 + a_1 ln(E_\gamma) + a_2 ln(E_\gamma)^2 + a_3 ln(E_\gamma)^3 + a_4 ln(E_\gamma)^4 + a_5 ln(E_\gamma)^5. \quad (5.2)$$

The activity of the ^{56}Co source was unknown at time of use, so it was scaled to the ^{152}Eu data over the overlap region 800 keV and 1400 keV. Uncertainty in the efficiency was calculated analytically from the uncertainty in the fit parameters, $a_0 - a_5$. Figure 5.3 shows the combined efficiency for the CLOVER detector located at 86°.

5.2 Gamma-ray Spectroscopy

The result of the post-processing described above is a two-dimensional histogram of add-backed, Compton suppressed γ-ray-energy vs. time since last *rf*. This histogram was separated into eight, 21 ns wide y-projections. Each of these projections correspond to a specific time since last *rf* time window. A y-projection for the time-integrated spectrum (0 ns - 169.3

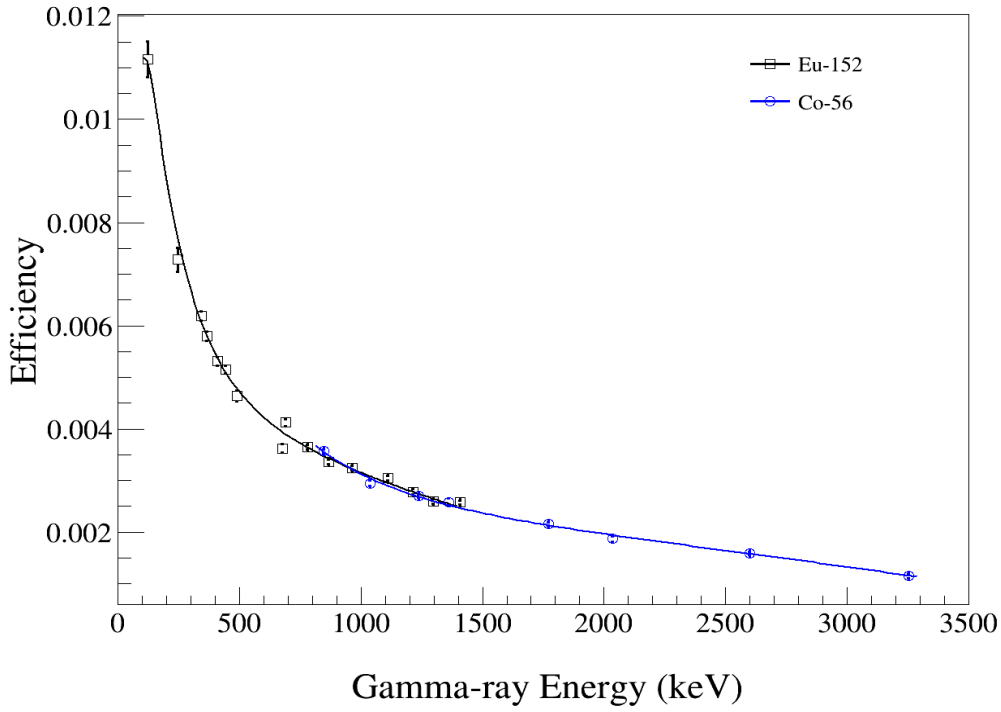

Figure 5.3: 86° CLOVER detection efficiency. Black data below 1400 keV is from a sealed ^{152}Eu source. Blue data above 1400 keV is from a house-made ^{56}Co source which was scaled to match the Eu data.

ns) acted as a master spectrum. For each γ-ray of interest, the peak was fit in the master spectrum using gf3 in the RadWare code package [49]. Effort was taken to include at least one nearby isolated peak in order to fix the relative peak widths. Once a satisfactory fit was obtained in the master spectrum, the peak positions and widths were fixed. This master fit was then applied to each of the eight sub-spectra. With the peak widths and positions fixed, the only free parameters were the peak heights and the background.

Figure 5.4 shows the added-back, Compton suppressed, time-integrated spectrum for the 86° CLOVER. The spectrum contains peaks from reactions on ^{35}Cl, ^{37}Cl, and ^{23}Na. The triangular shaped peaks at 563, 596, 834, 1039, 1204, and 1463 keV are the result of inelastic scattering on Germanium in the CLOVER. As the Ge nucleus recoils from the impact, it can de-excite via γ-emission resulting in a γ-ray feature with this characteristic shape. The red labels indicate lines that were used in the analysis described in the next section.

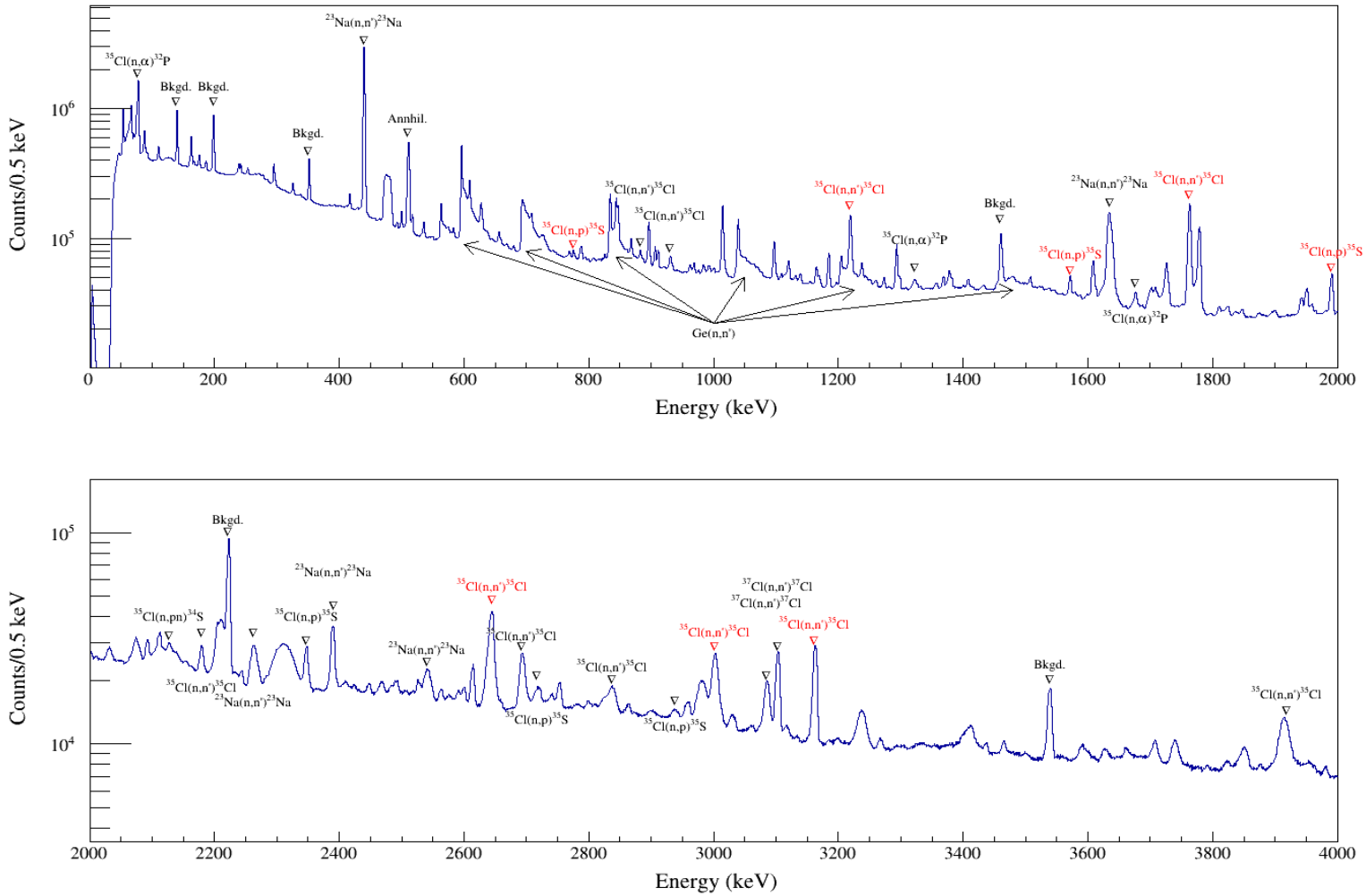

Figure 5.4: Added-back, Compton suppressed, time-integrated γ-ray spectrum for the 86° CLOVER. Red labels indicate lines that were used in the analysis described in this chapter.

5.3 Gamma-ray Production Results

Gamma-ray production as a function of time-since-last *rf* was determined for the γ-rays of interest. These results were compared to CoH_3 calculations provided by Toshihiko Kawano at Los Alamos National Laboratory (LANL). The successor to the popular GNASH code, CoH_3 is a statistical Hauser-Feshbach code used for calculating compound nuclear reactions for medium to heavy nuclei [32]. As discussed in Section 1.3, little experimental data exist in the MeV range for the $^{35}\mathrm{Cl}(n,p)^{35}\mathrm{S}$ cross section reaction and thus evaluators were forced to rely heavily on theoretical results such as those provided by COH_3. The result is an over-prediction in the ENDF/B-VIII.0 evaluation library for this channel when compared to recent results such as those by Kuvin et. al. and this thesis. The CoH_3 results used in this thesis are Dr. Kawano's best attempt to match the $^{35}\mathrm{Cl}(n,p)$ channel to Kuvin's results as closely as possible [39].

Because of the frame overlap issue discussed in Section 3.4, γ-ray production vs. time-since-last-*rf* is the most natural space in which to compare the experimental and theoretical data. A flux matrix, 2D histogram of time-since last-*rf*, was built to have the same time binning as the gamma ray data. That is, the 170 ns *rf* period was divided up into fifteen equally sized time windows. The CoH_3 angle-integrated γ-ray production cross sections were converted to total γ-ray production values per time bin. This was done by determining the total γ-rays of interest produced for each bin in the flux matrix according to,

$$P^{\gamma}_{bin} = \sigma^{\gamma}(E)\phi_{bin}\rho_A\Omega It \tag{5.3}$$

where P^{γ}_{bin} is the number of the γ-rays produced for the given flux matrix bin, $\sigma^{\gamma}(E)$ is the CoH_3 cross section for production of this γ-ray at the energy of the flux matrix bin, ϕ_{bin} is the bin content from the flux matrix, ρ_A is the target areal atom density of ^{35}Cl, Ω is the target solid angle, and It is the experimental integrated beam current.

The results for the individual γ-rays can be combined to yield a powerful metric for the total channel cross section. This method, called the method of parallel paths, involves adding together partial γ-ray cross sections for as many parallel (non-coincident) transitions as possible. This sum is compared to theoretical equivalent [5],

$$\sigma(n,n') = \sum_{\gamma_i} \sigma^{exp}(n,n'\gamma_i)\frac{\sigma^{CoH}(n,n')}{\sum_{\gamma_i}\sigma^{CoH}(n,n'\gamma_i)}. \tag{5.4}$$

If the strongest low-lying lines are used, the majority of the total channel cross section will be captured by this sum. Optical model and Hauser-Feshbach calculations are good at estimating average values such as the total channel cross section, but may not accurately

reproduce detailed nuclear structure quantities such as specific state-to-state transition rates, due to a lack of complete knowledge of the discrete level scheme. The parallel paths method thus allows calculation of the total channel cross section, based on a limited number of partial cross sections.

Gamma-ray angular distributions

Gamma-ray emission is not isotropic but has a characteristic angular dependence based on the transition multipolarity. The γ-ray production cross section at a given angle θ is related to the angle-integrated cross section by an angular distribution correction factor W(θ) by the relation [31],

$$\sigma(\theta) = \sigma W(\theta). \tag{5.5}$$

The correction factor W(θ) can be expanded in a basis of Legendre polynomials as

$$W(\theta) = 1 + A_2 P_2(cos\theta) + A_4 P_4(cos\theta). \tag{5.6}$$

The expansion coefficients, A_k are referred to as the anisotropy coefficients and are a function of the populations of the magnetic sub-states. These are captured by a population tensor $\rho_k(\mathbf{J})$ and the multipolarity mixing ratio δ_γ. The coupling of initial, final, and γ-ray angular momentum are captured by the Racah coefficient W($\mathbf{J}_i, \mathbf{J}_i, \mathbf{L}_1, \mathbf{L}_2; k\mathbf{J}_f$). Under the condition that the magnetic substates are symmetrically populated, P$_m(\mathbf{J})$ = P$_{-m}(\mathbf{J})$, the anisotropy coefficients can be determined by referencing tables compiled by Yamazaki [59]. However, in practice the actual m-state alignment will be attenuated which reduces the magnitude of the anisotropy. This is captured by introducing attenuation coefficients a_k,

$$A_k(\mathbf{J}_i\mathbf{L}_1\mathbf{L}_2\mathbf{J}_f) = a_k(\mathbf{J}_i) A_k^{max}(\mathbf{J}_i\mathbf{L}_1\mathbf{L}_2\mathbf{J}_f). \tag{5.7}$$

Unfortunately, these attenuation factors are a function of the specific formation process of the state as well as the state lifetime and are not readily calculable. For the experiment presented here, only two angles were available, 86° and 42°. Meaning that there is only one equation (the ratio of the 86° and 42° data) and two unknowns. It is possible to assume a theoretical distribution of the m-states (e.g. Gaussian) to reduce the number of unknowns to one and then solve for the angular distribution. However, in this thesis the γ-ray data has been left as is.

$^{35}\mathbf{Cl}(n, n'\gamma)^{35}\mathbf{Cl}$

Table 5.1 lists inelastic scattering lines for ^{35}Cl that were observed. Observed, but non-parallel lines were not used in the parallel-paths sum. Two parallel lines, 2693.6 keV and 3918.4 keV were not used. These were not included because contamination from other strong γ-rays at the same energy prevented obtaining reliable peaks fits.

E_i	J_i^π	E_γ	E_f	J_f^π	Type	Used
1219.29	$1/2^+$	1219.3	0.0	$3/2^+$	parallel	used
1763.04	$5/2^+$	1763.13	0.0	$3/2^+$	parallel	used
2645.74	$7/2^+$	882.84	1763.04	$5/2^+$	non-parallel	not used
2645.74	$7/2^+$	2645.7	0.0	$3/2^+$	parallel	used
2693.75	$3/2^+$	930.9	1763.04	$5/2^+$	non-parallel	not used
2693.75	$3/2^+$	2693.6	0.0	$3/2^+$	parallel	not used
3002.3	$5/2^+$	3002.4	0.0	$3/2^+$	parallel	used
3162.8	$7/2^-$	517.2	2645.74	$7/2^+$	non-parallel	not used
3162.8	$7/2^-$	3162.5	0	$3/2^+$	parallel	used
3918.4	$3/2^+$	3918.4	0	$3/2^+$	parallel	not used

Table 5.1: Observed γ-ray lines from inelastic scattering on ^{35}Cl. The last column indicates which transitions were used to represent the (n,n') channel via the parallel paths method.

Figures 5.5a-5.5e, show the γ-ray production results. In each figure, the red triangles represent the data from the CLOVER positioned at 86°, the blue squares represent the data from the CLOVER positioned at 42°, and the black circles represent the CoH_3 data. The 42° data is always higher than the 86° data due to the anisotropy of γ-radiation. The uncertainty in the experimental neutron yield was determined analytically from the uncertainty in the peak area and the uncertainty in the efficiency. Uncertainty in the CoH_3 neutron yield is from the flux uncertainty. The CoH_3 cross section values were assumed to have no uncertainty and uncertainties resulting from the target mass or integrated current were negligible. For both the experimental and CoH_3 points, the TOF error bars represent TOF bin widths, not uncertainty in the TOF.

For each CLOVER, a χ^2 was calculated between that CLOVER and the CoH_3 data to obtain a metric for the shape goodness-of-fit. The 42° CLOVER was further away from the target and thus had lower statistics and large resultant error bars. The reduced $\tilde{\chi}^2$ is given in the figures, where the number of degrees of freedom was taken as eight, the number of TOF windows. For most cases the $\tilde{\chi}^2$ was less than one, indicating very good agreement in shape with the CoH_3 data. While these are γ-ray production plots and thus the shape is primarily determined by the shape of the neutron flux, inconsistencies between experimental and theoretical cross section shapes are still visible. This is apparent in Figure 5.5a, the case of the 1219 keV line. Here, the experimental γ-ray production does not have a systematic

offset from the theoretical data, but is low at low TOF and high at high TOF. This indicates that the CoH_3 cross section is too low at low energy and too high at high energy. This inconsistency results in the much higher $\tilde{\chi}^2$s of 5.3. For all cases, the last TOF bin (≈160 ns) begins to deviate from CoH_3. This bin is wrapped, containing contributions from 3 MeV and 10-12 MeV. See Figure 3.6.

The parallel paths sum for the five transitions is shown in Figure 5.6. The total experimental inelastic channel γ-ray production is roughly 30% higher than that predicted by CoH_3.

$^{35}\mathbf{Cl}(n,p\gamma)^{35}\mathbf{S}$

Table 5.1 lists the $^{35}\mathrm{Cl}(n,p\gamma)^{35}\mathrm{S}$ lines that were observed.

E_i	J_i^π	E_γ	E_f	J_f^π	Type	Used
1572.378	$1/2^+$	1572.334	0	$3/2^+$	parallel	used
1991.28	$7/2^-$	1991.28	0	$3/2^+$	parallel	used
2347.789	$3/2^-$	775.398	1572.378	$1/2^+$	non-parallel	not used
2347.789	$3/2^-$	2347.69	0	$3/2^+$	parallel	used

Table 5.2: Observed γ-ray lines from reaction on ^{35}S.

Figures 5.7a-5.7c, show the γ-ray production results. Again, the 42° data is always higher than the 86° data due to the anisotropy of γ-radiation and due to poor statistics the 42° CLOVER data has a large uncertainty. The $\tilde{\chi}^2$ was noticeably higher than in the (n,p) case indicating poor agreement between the experimental and theoretical cross section shapes.

The parallel paths sum for the five transitions is shown in Figure 5.6. The total experimental (n,p) channel γ-ray production is roughly 15% higher than that predicted by CoH_3. The closeness of these two results is encouraging for the evaluation and will be discussed in the Conclusions chapter.

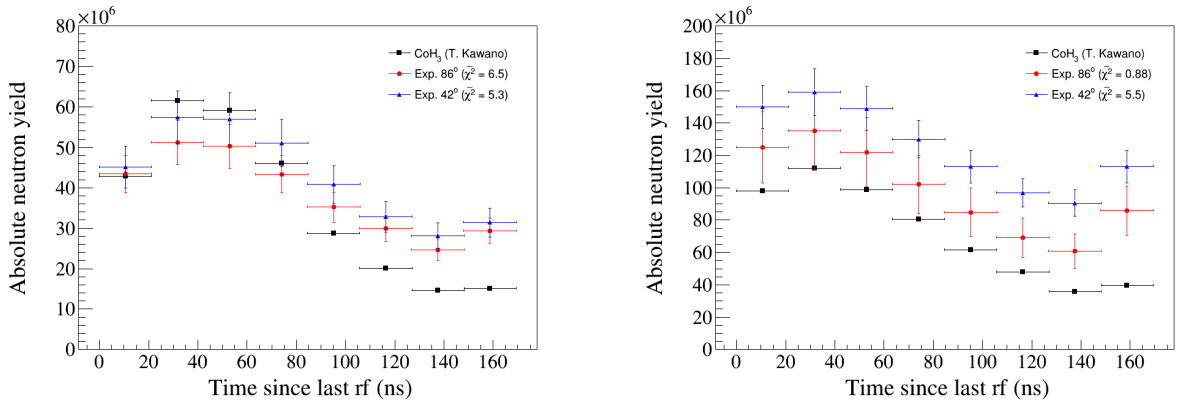

(a) 1219 keV

(b) 1763 keV

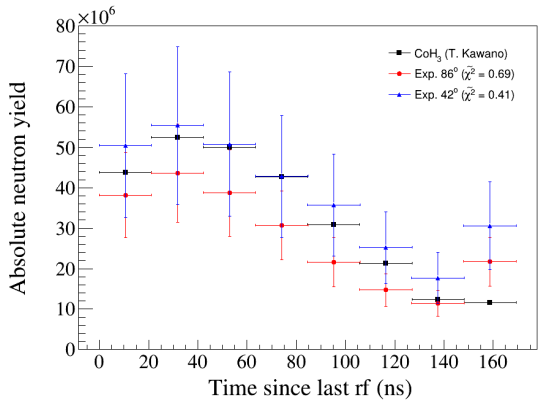

(c) 2645 keV

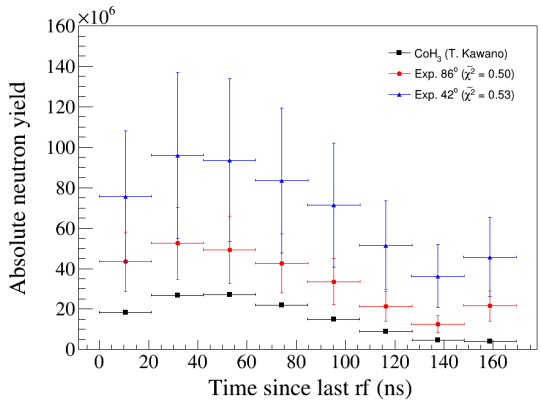

(d) 3002 keV

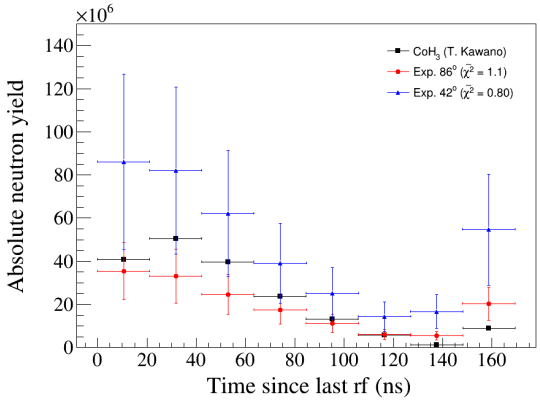

(e) 3163 keV

Figure 5.5: Gamma-ray production vs. time-since-last *rf* for five of the first six parallel inelastic transitions.

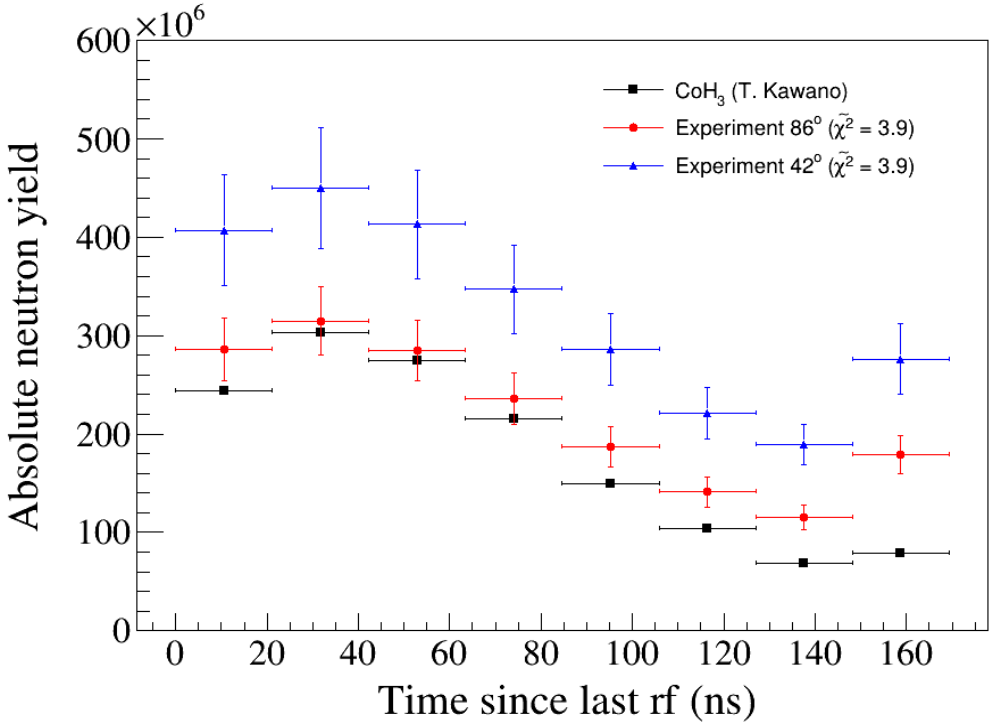

Figure 5.6: Parallel paths sum of the 1219, 1763, 2645, 3002, and 3163 keV lines in ^{35}Cl.

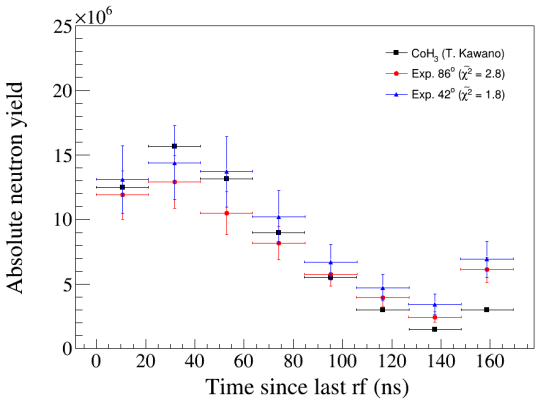

(a) 1572 keV

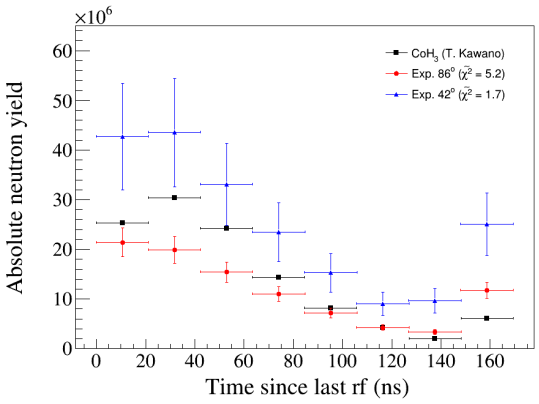

(b) 1991 keV

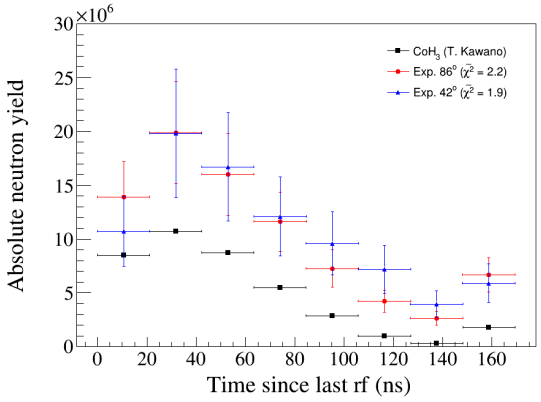

(c) 2347 keV

Figure 5.7: Gamma-ray production vs. time-since-last *rf* for the first three parallel (n,p) transitions.

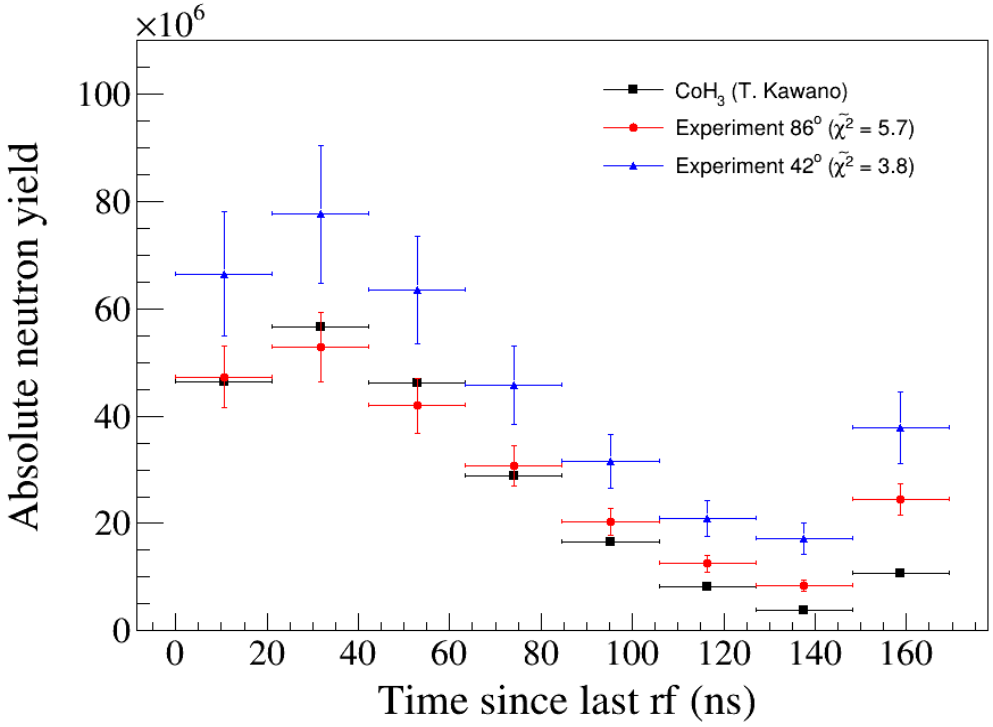

Figure 5.8: Parallel paths sum of the 1572, 1991, and 2347 keV lines in ^{35}S

Chapter 6

Activation Analysis and Results

6.1 Introduction

Cross section determination via activation is an inherently energy-integrated process. This is in contrast to in-beam target (GENESIS) or active target (CLYC) type methods which can be used to produce energy differential cross sections. The benefit of activation is that as a comparatively simple technique, it provides a reliable check on the results obtained via other methods. [4]

6.2 Experimental Setup

Two 1.3 cm diameter, NaCl targets were prepared in an identical manner to that used in the GENESIS portion. One target (0.4634(8) g/cm^2) served as the primary in-beam target. It was secured to the Mylar face of the beampipe which passes through the shielding wall between the cyclotron vault and Cave 5. See Figure 6.1. This position is just downstream of the collimator. The second target (0.4577(11) g/cm^2) was used as an out-of-beam reference and placed about one foot below the in-beam target. An out-of-beam reference was required because our flux measurement system, STOF, is located in Cave 5 while the target was located in the vault. Because the activation target was in close proximity to the breakup source, collimator, and surrounding equipment, the activation target likely sees a large scattered flux component not seen by STOF. It was assumed that both targets see the same scattered flux component and thus the reference activation can be subtracted from the primary target activation. The primary target was irradiated for approximately four days at 14 μA for a total of 4.72×10^6 μC of beam.

Figure 6.1: In-beam target location. Target was attached to the Mylar face of the beampipe between the cyclotron vault and Cave 5. Figure is looking downstream. Collimator is visible on lower right hand corner. The out-of-beam target is not visible.

6.3 Analysis

Following conclusion of the experiment the targets were removed and placed in storage for a week to allow any short-lived reaction products to decay away.

Possible contaminating reactions

To determine what reaction products would be present in the NaCl sample after irradiation, a review of all possible reactions was completed. All energetically allowed reactions, given the limited energy range of neutrons produced from breakup of 14 MeV deuterons on graphite, are listed in the following tables: Table 6.1 for ^{35}Cl, Table 6.2 for ^{37}Cl, and Table 6.3 for ^{23}Na. Reactions that produce activation products with half-lives greater than a few days that would be present after the post-experiment waiting period are highlighted in gray. All told, six reactions meet this criteria. They are: ^{35}Cl(n,γ)^{36}Cl, ^{35}Cl(n,^{3}He)^{33}P, ^{37}Cl(n,nα)^{33}P, ^{37}Cl(n,t)^{35}S, ^{37}Cl(n,2n)^{36}Cl, and ^{23}Na(n,2n)^{22}Na. Two reactions produce ^{36}Cl which has half-life of 3.01×10^5 years and thus is too long-lived to be noticeable. The remaining

four reactions have relatively high thresholds (8-13 MeV) and have very low reaction cross sections. Thus these can be safely ignored as well. The result is that the only activation products left after the waiting period are ^{35}S and ^{32}P corresponding to the ^{35}Cl(n,p) and ^{35}Cl(n,α) reactions respectively.

Reaction	Threshold (MeV)	Half-life
^{35}Cl(n,γ)^{36}Cl	0	3.01×10^5 y
^{35}Cl(n,α)^{32}P	0	14.268 d
^{35}Cl(n,p)^{35}S	0	87.37 d
^{35}Cl(n,n')^{35}Cl	0	Stable
^{35}Cl(n,d)^{34}S	4.26591	Stable
^{35}Cl(n,np)^{34}S	6.55468	Stable
^{35}Cl(n,nα)^{31}P	7.19986	Stable
^{35}Cl(n,pα)^{31}Si	7.92949	157.36 m
^{35}Cl(n,2α)^{28}Al	9.19937	2.245 m
^{35}Cl(n,t)^{33}S	9.57474	Stable
^{35}Cl(n,^{3}He)^{33}P	9.8113	25.35 d
^{35}Cl(n,2p)^{34}P	11.2881	12.43 s
^{35}Cl(n,dα)^{30}Si	12.41823	Stable
^{35}Cl(n,2n)^{34}Cl	13.00969	32 m (isomer)

Table 6.1: Possible reactions on ^{35}Cl. Highlighted rows indicate which activation products will be present after the two week wait.

Liquid scintillation counting

Liquid scintillation counting is necessary because the two activation products of interest (^{35}S and ^{32}P) decay entirely via low-energy β-emission ($Q_\beta^{35S} = 167$ keV; $Q_\beta^{32P} = 1710$ keV) to the ground state of the daughter. Each of the two NaCl pellets were dissolved in 4 ml of water and then mixed with 16 ml of Ultima Gold XR scintillation cocktail. An unirradiated NaCl sample was also prepared in order to determine the background. All three samples (in-beam, out-of-beam, and unirradiated) were then counted periodically over a 250 day

Reaction	Threshold (MeV)	Half-life
^{37}Cl(n,γ)^{38}Cl	0	37.24 m
^{37}Cl(n,n')^{37}Cl	0	Stable
^{37}Cl(n,α)^{34}P	1.6092	12.43 s
^{37}Cl(n,p)^{37}S	4.19424	5.05 m
^{37}Cl(n,d)^{36}S	6.33003	Stable
^{37}Cl(n,nα)^{33}P	8.0634	25.35 d
^{37}Cl(n,np)^{36}S	8.61533	Stable
^{37}Cl(n,t)^{35}S	10.06121	87.37 d
^{37}Cl(n,2n)^{36}Cl	10.59235	3.01×10^5 y
^{37}Cl(n,2α)^{30}Al	13.0220	3.62 s
^{37}Cl(n,pα)^{33}Si	13.2417	6.11 s

Table 6.2: Possible reaction on ^{37}Cl. Highlighted rows indicate which activation products will be present after the two week wait.

period in a TriCarb 2910 TR LSC from Perkin Elmer [23] at the University of California, Berkeley. The LSC was previously calibrated by Batchelder *et al.* using standard vials of ^{3}H and ^{14}C as well as a prepared 100 nCi ^{35}S sample. The reported efficiencies are 92.7(7)% for ^{35}S and 100% for ^{32}P [4]. Figure 6.2 shows the subtracted decay rate data for the in-beam target. Assuming only ^{35}S and ^{32}P are present, the decay curve follows the following double exponential

$$A(t) = A_{S0}e^{-\lambda_S t}\epsilon_S + A_{P0}e^{-\lambda_P t}\epsilon_P \tag{6.1}$$

where, A_{S0} and A_{P0} are the initial activities, λ_S and λ_P are the decay constants, and ϵ_S and ϵ_P are the detection efficiencies of ^{35}S and ^{32}P respectively. The $\chi^2/d.o.f.$ was 7.33, indicating a good fit and validating the assumption that there was no significant contribution from contaminating reactions.

Correction for sample decay during experiment

Activation products decay continuously, including during the course of the experiment. This must be taken into account to obtain an accurate value for the total number of reactions that occurred. The number of activation products at the end of irradiation assuming no decay

Reaction	Threshold (MeV)	Half-life
^{23}Na(n,γ)^{24}Na	0	14.997 h
^{23}Na(n,n')^{23}Na	0	Stable
^{23}Na(n,p)^{23}Ne	3.75122	37.24 s
^{23}Na(n,α)^{20}F	4.03571	11.07 s
^{23}Na(n,d)^{22}Ne	6.857945	Stable
^{23}Na(n,np)^{22}Ne	9.18017	Stable
^{23}Na(n,nα)^{19}F	10.92684	Stable
^{23}Na(n,t)^{21}Ne	11.14527	Stable
^{23}Na(n,2α)^{16}N	12.5187	7.13 s
^{23}Na(n,2n)^{22}Na	12.96501	2.6018 y

Table 6.3: Possible reaction on ^{23}Na. Highlighted rows indicate which activation products will be present after the two week wait.

(N_0^{nd}) can be determined from the number of activation products at the end of irradiation assuming decay (N_0^d), which was obtained from the LSC data. During irradiation, the number of activation products follows the well-known build-up and decay equation,

$$N(t)^d = \frac{R}{\lambda}(1 - e^{-\lambda t}) \tag{6.2}$$

where, R is the (constant) reaction rate and λ is the decay constant of the activation product. If there was no decay, the number of activation products would simply be,

$$N(t)^{nd} = Rt. \tag{6.3}$$

If t_1 is the time at the end of irradiation, then

$$N_0^d = \frac{R}{\lambda}(1 - e^{-\lambda t1})$$
$$N_0^{nd} = Rt_1.$$

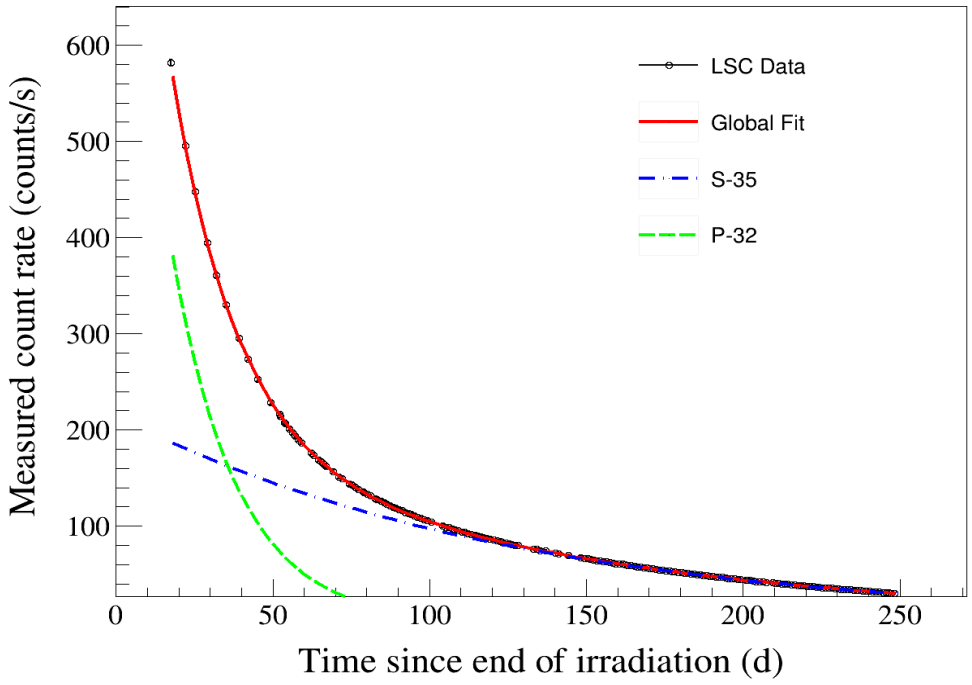

Figure 6.2: In-beam activation decay data. $\chi^2/d.o.f. = 7.33$

Thus, we obtain for the number of activation products at the end of irradiation (assuming no decay),

$$N_0^{nd} = \frac{N_0^d \lambda t_1}{1 - e^{-\lambda t_1}}. \tag{6.4}$$

This is a convenient analytical result. However, in reality the production rate R was not constant due to fluctuations in cyclotron beam current, as well as down periods such as those for mid-experiment calibration and the twice daily liquid nitrogen fills. The cyclotron Beam Current Monitor (BCM) records beam current once every minute. The ratio of reactions without decay to that with decay was calculated from the BCM data by assuming one minute long isolated pulses. Each pulse was assumed to not decay during the pulse. Production for each pulse was summed and then divided by the LSC determined number of reactions. Since the half-life of ^{35}S is 87.37 days, for a four day long experiment, the relative amount decayed during the irradiation period should be small. The ratio assuming no decay to that with decay was 1.0183 when calculated using equation 6.4 and 1.0188 when calculated from the BCM data. Both values are close to one as expected. For ^{32}P, half-life of 14.27 days, the

analytical ratio is 1.118 and the BCM ratio is 1.116. This again confirms the approximate validity of equation 6.4. The BCM values were used to correct the data for decay.

6.4 Uncertainty Quantification

The various uncertainties involved are listed in Table 6.4. The dominant systematic uncertainty was from the neutron flux. The uncertainty in the expected activation, as determined by convolving the flux uncertainty with the CoH_3 cross section was 2%. The flux, as mentioned in Section 3.4, could only be measured down to about 1.75 MeV. Below this point, no data is available and the flux was assumed to be zero in the analysis. While this is strictly incorrect, if it is assumed that the flux falls smoothly to zero, then the area below 1.75 MeV only accounts for 2% of the total flux. See Figure 3.3. Thus, a 2% systematic uncertainty was added. A more difficult systematic uncertainty to quantify is the assumption that the in-beam and out-of-beam targets see the same scattered flux which was used to justify subtracting the out-of-beam activation from the in-beam data. It was assumed to have zero uncertainty. The provided CoH_3 cross sections were assumed to have zero uncertainty at the given energy points, However, interpolation was required between given data points and an additional 1% uncertainty was therefore included. The uncertainties listed in Table 6.4 were added in quadrature to obtain the final value of 3.6%.

Uncertainty source	Value	Type
Flux above 1.75 MeV	2%	Systematic
Lack of flux below 1.75 MeV	2%	Systematic
Interpolation of CoH XS	<1%	Systematic
Solid angle	<1%	Systematic
Integrated beam current	<1%	Systematic
LSC efficiency	1%	Systematic
Target masses, half-lives	<<1%	Systematic
LSC count data	<1%	Statistical

Table 6.4: Sources of Uncertainty in the activation analysis. Uncertainties from the measured neuron flux were the dominant systematic source.

6.5 Results

The above analysis returns a value for the total number of reactions observed. This number can be compared to that expected using our known flux and a provided cross section. As with the γ-ray analysis in Chapter 5, CoH_3 calculation provided by Toshiko Kawano were used for comparison. For both reactions of interest, the ratio of activation to that expected by calculation were determined. Table 6.5 list the results. A ratio of 0.90 was seen for the ^{35}Cl(n,α_{tot}) reaction. Thus ten percent less activity than expected from activation was seen. A ratio of 1.16 was seen for the ^{35}Cl(n,p_{tot}) reaction. Thus sixteen percent more activity than expected from activation was seen.

Reaction	Ratio	XS source
^{35}Cl(n,p$_{tot}$)	1.16±0.04	CoH
^{35}Cl(n,α_{tot})	0.89±0.03	CoH

Table 6.5: Activation results. The ratio is that of the experimental activation to that expected by theoretical calculation.

Chapter 7

Conclusions

7.1 The Nuclear Data Pipeline

The nuclear reaction data evaluation process (pipeline) can be broken down into four steps: compilation, evaluation, processing, and validation [6]. The first step, compilation involves compiling all experimental data for the reaction under consideration. The compiled data is tabulated in the Experimental Nuclear Reaction Data Library (EXFOR). The second step, evaluation, involves studying the compiled data and rejecting discrepant data or adjusting data as needed to ensure an accurate evaluation. No experiment will cover all energies and all reaction channels. Even worse, because ENDF is mainly used for nuclear energy, national security, and international counterproliferation applications, most data is for thermal (25 meV) or fusion (14 MeV) energies [6]. However, transport codes used for applications (e.g. Serpent, MCNP) require cross section values for all channels at all energies. Evaluators accomplish this by using the experimental data to inform and constrain model calculations. The third step is processing which involves converting the evaluated cross sections into a form that engineers and scientists can use. The last step involves validating the new evaluation against integral benchmark data.

The model calculations mentioned above involve a large number of free parameters. If little experimental data exists to constrain the model, then the results may be unreliable. This thesis has presented a new style of cross section measurement in which the experiment was designed with the evaluator in mind. Instead of measuring a single channel we have measured multiple channels simultaneously, thereby providing a stronger constraint for the evaluator. This is especially important in the case in which the measured cross section differs significantly from the current evaluation (e.g $^{35}\mathrm{Cl}(n, p_0)$). In cases such as this, the evaluator must make large changes in model parameters to account for the discrepancy. Since total evaluated cross section is conserved, the magnitude of other channel(s) will necessarily change.

7.2 Results and Theoretical Implications

Chapter 4 described a measurement of the (n, p_0) channel. The obtained cross section was roughly half of the ENDF/B-VIII.0 evaluation. Evidence of this discrepancy was previously reported by Kuvin and Batchelder. CoH_3 model calculations were performed by Toshihiko Kawano at LANL, for which the model was adjusted to match the Kuvin results as closely as possible. Due to the conserved total cross section, other channel(s) must necessarily increase. The CoH_3 results were compared against the γ-ray and activation measurements described in Chapters 5 and 6 respectively.

Gamma-ray production results were summed according to the parallel paths method. For a light nucleus such as ^{35}Cl with a low level density, only a small number of observed γ-rays are needed to account for the majority of the channel strength. The γ-ray production results indicate that the CoH_3 model under-predicts the strength of the $(n, p\gamma)$ channel by 15%. The γ-ray production results also indicate that the CoH_3 model under-predicts the strength of the $(n, n'\gamma)$ channel by 30%. Activation confirms the underestimation of the (n, p_{tot}) channel as well as the over-prediction of the (n, α_{tot}) channel by 11%.

The knowledge of these channel strengths can now be used by the evaluator to refine model. Possible model changes include an increase in the imaginary part of the neutron optical potential, allowing increased non-elastic strength (and decreased elastic strength). Reaction model codes such as CoH_3 allow the user to vary all optical model parameters, including those for neutrons and protons independently. Recalling from Section 2.2 that the optical model provides the transmission coefficients used in the Hauser-Feshbach formalism to determine the compound nucleus decay modes, careful adjustment of the relative imaginary well depths for neutrons and protons can be used to vary the (n, n') and (n, p) magnitudes.

7.3 Future Work

There are several aspects of this work that could be improved in future studies. The first is the γ-ray angular distributions. With only two angles, it was not possible in this thesis to correct for the γ-ray anisotropy without invoking a functional assumption of the relative m-state populations. An increase in the number of HPGe detectors would allow direct measurement of the attenuation coefficients. Fortunately, seven new HPGes have been purchased for the GENESIS project providing this capability for the future. Further model constraint could be accomplished by performing a measurement of the $^{35}\mathrm{Cl}(p, p'\gamma)$ cross section which would help to constrain the proton optical model parameters. Lastly, work performed during the conduct of this thesis project (though not presented here) has shown that CLYC can be used as a neutron flux monitor. The process is near identical to that used to calculate the $^{35}\mathrm{Cl}(n, p_0)$ cross section. From the number of observed $^{6}\mathrm{Li}(n, \alpha)$t events and the known cross section for this reaction, the flux can be calculated. This method requires accurate knowledge of the detection efficiency and downscatter effects in CLYC. However this method

is still subject to wraparound effects and thus the accessible energy range is limited. The horizontal ^{6}Li(n,α)t band visible in Figure 4.8, which is largely due to the 240 keV resonance can be used to obtain a single low energy data point. A final improvement can be accomplished using advanced waveform processing for CLYC. This method, currently under development, has been proven to allow separation of the proton and alpha producing reactions. This would allow access to the, currently unavailable, first wraps and thereby extension of the measured cross section to lower energies. This has the added benefit of removing the wrapped Li bands from the unwrapped ^{35}Cl(n,p_0) band. These wraps are currently a source of background increasing the uncertainty in the χ^2 minimization fit routine.

Bibliography

[1] *725 and 730 DPP-PSD: Register Description and Format*. https://www.caen.it/products/dpp-psd/. CAEN Technologies. Apr. 2023.

[2] S. Agostinelli et al. "Geant4 – a simulation toolkit". In: *Nuclear Instruments and Methods in Physics Research Section A: Accelerators, Spectrometers, Detectors and Associated Equipment* 506.3 (2003), pp. 250–303. ISSN: 0168-9002. DOI: https://doi.org/10.1016/S0168-9002(03)01368-8.

[3] Mauricio Ayllon et al. "Design, construction, and characterization of a compact DD neutron generator designed for 40Ar/39Ar geochronology". In: *Nuclear Instruments and Methods in Physics Research Section A: Accelerators, Spectrometers, Detectors and Associated Equipment* 903 (2018), pp. 193–203. ISSN: 0168-9002. DOI: https://doi.org/10.1016/j.nima.2018.04.020. URL: https://www.sciencedirect.com/science/article/pii/S0168900218305102.

[4] J. C. Batchelder et al. "Possible evidence of nonstatistical properties in the ^{35}Cl$(n,p)^{35}$S cross section". In: *Phys. Rev. C* 99 (4 Apr. 2019), p. 044612. DOI: 10.1103/PhysRevC.99.044612. URL: https://link.aps.org/doi/10.1103/PhysRevC.99.044612.

[5] L.A. Bernstein et al. "Pu-239(n,2n)Pu-238 cross section deduced using a combination of experiment and theory". In: *Phys. Rev. C* 65 (Feb. 2002). DOI: 10.1003/PhysRevC.65.021601.

[6] Lee A. Bernstein et al. "Our Future Nuclear Data Needs". In: *Annual Review of Nuclear and Particle Science* 69.1 (2019), pp. 109–136. DOI: 10.1146/annurev-nucl-101918-023708. eprint: https://doi.org/10.1146/annurev-nucl-101918-023708. URL: https://doi.org/10.1146/annurev-nucl-101918-023708.

[7] Raymond T. Birge. "The Calculation of Errors by the Method of Least Squares". In: *Phys. Rev.* 40 (2 Apr. 1932), pp. 207–227. DOI: 10.1103/PhysRev.40.207. URL: https://link.aps.org/doi/10.1103/PhysRev.40.207.

[8] D.L. Bleuel et al. "Characterization of a tunable quasi-monoenergetic neutron beam from deuteron breakup". In: *Nuclear Instruments and Methods in Physics Research Section B: Beam Interactions with Materials and Atoms* 261.1 (2007). The Application of Accelerators in Research and Industry, pp. 974–979. ISSN: 0168-583X. DOI: https:

//doi.org/10.1016/j.nimb.2007.04.125. URL: https://www.sciencedirect.com/science/article/pii/S0168583X07009238.

[9] Alessandro Borella et al. "Characterization and Monte Carlo simulations for a CLYC detector". In: *Int. J. Mod. Phys. Conf. Ser.* 48 (2018). Ed. by Anna Erickson, Adam Bernstein, and Marianne Hamm, p. 1860115. DOI: 10.1142/S2010194518601151.

[10] D.A. Brown et al. "ENDF/B-VIII.0: The 8th Major Release of the Nuclear Reaction Data Library with CIELO-project Cross Sections, New Standards and Thermal Scattering Data". In: *Nuclear Data Sheets* 148 (2018). Special Issue on Nuclear Reaction Data, pp. 1–142. ISSN: 0090-3752. DOI: https://doi.org/10.1016/j.nds.2018.02.001. URL: https://www.sciencedirect.com/science/article/pii/S0090375218300206.

[11] Rene Brun and Fons Rademakers. "ROOT — An object oriented data analysis framework". In: *Nuclear Instruments and Methods in Physics Research Section A: Accelerators, Spectrometers, Detectors and Associated Equipment* 389.1 (1997). New Computing Techniques in Physics Research V, pp. 81–86. ISSN: 0168-9002. DOI: https://doi.org/10.1016/S0168-9002(97)00048-X. URL: https://www.sciencedirect.com/science/article/pii/S016890029700048X.

[12] Richard F. Casten. *Nuclear Structure from a Simple Perspective*. Great Clarendon Street, Oxford OX2 6DP: Oxford University Press, 2000.

[13] Jun Chen, John Cameron, and Balraj Singh. "Nuclear Data Sheets for A = 35". In: *Nuclear Data Sheets* 112.11 (2011), pp. 2715–2850. ISSN: 0090-3752. DOI: https://doi.org/10.1016/j.nds.2011.10.001. URL: https://www.sciencedirect.com/science/article/pii/S0090375211000950.

[14] T. Cisneros. *MCFR System Description*. Private Communication. July 2022.

[15] *CLYC Gamma-Neutron Scintillator*. Accessed 5 March 2024. Radiation Monitoring Devices. 2024. URL: https://www.rmdinc.com/product-category/products/clyc-gamma-neutron-scintillators/.

[16] *CoMPASS: Multiparametric DAQ Software for Physics Applications*. "https://www.caen.it/products/compass/. CAEN Technologies. Nov. 2023.

[17] N. D'Olympia et al. "Fast neutron response of ^{6}Li-depleted CLYC detectors up to 20MeV". In: *Nuclear Instruments and Methods in Physics Research Section A: Accelerators, Spectrometers, Detectors and Associated Equipment* 763 (2014), pp. 433–441. ISSN: 0168-9002. DOI: https://doi.org/10.1016/j.nima.2014.06.074. URL: https://www.sciencedirect.com/science/article/pii/S0168900214008286.

[18] N. D'Olympia et al. "Pulse-shape analysis of CLYC for thermal neutrons, fast neutrons, and gamma-rays". In: *Nuclear Instruments and Methods in Physics Research Section A: Accelerators, Spectrometers, Detectors and Associated Equipment* 714 (2013), pp. 121–127. ISSN: 0168-9002. DOI: https://doi.org/10.1016/j.nima.2013.02.043. URL: https://www.sciencedirect.com/science/article/pii/S0168900213002349.

[19] T. W. Donnelly et al. *Foundations of Nuclear and Particle Physics*. Cambridge CB2 8BS, United Kingdom: Cambridge University Press, 2017.

[20] F. Patrick Doty et al. *Elpasolite scintillators*. Tech. rep. SAND2012-9951 463657. Sandia National Laboaratory, Dec. 2012. DOI: 10.2172/1096473. URL: https://www.osti.gov/biblio/1096473.

[21] *DT5730/DT5725: 8 Channel 14-bit 500/250 MS/s Digitizer*. https://www.caen.it/products/dt5725/. CAEN Technologies. Mar. 2023.

[22] J. J. Duderstadt and L. J. Hamilton. *Nuclear Reactor Analysis*. 111 River Street, Hoboken, NJ 07030: John Wiley & Sons, 1976.

[23] Perkin Elmer. *Tri-Carb 2910TR Low Activity Liquid Scintillation Analyzer*. Accessed 5 March 2024. 2014. URL: https://resources.perkinelmer.com/corporate/cmsresources/images/46-73886spc_tricarb2910trlsa.pdf.

[24] P. Fröbrich and R. Lipperheide. *Theory of Nuclear Reactions*. Great Clarendon Street, Oxford OX2 6DP: Oxford University Press, 1996.

[25] Jess C Gehin et al. *Fast Spectrum Molten Salt Reactor Options*. Tech. rep. ORNL/TM-2011/105. Oak Ridge National Laboratory, 2011. DOI: 10.2172/1018987. URL: https://www.osti.gov/biblio/1018987.

[26] J. M. Gordon et al. "GENESIS: Gamma Energy Neutron Energy Spectrometer for Inelastic Scattering". In: *Nuclear Instruments and Methods in Physics Research. Section A, Accelerators, Spectrometers, Detectors and Associated Equipment* 1061 (Apr. 2024). ISSN: 0168-9002. DOI: 10.1016/j.nima.2024.169120. URL: https://www.osti.gov/biblio/2283123.

[27] *H13795-100 (R13435-100 Hybrid Assembly)*. Hamamatsu Photonics. Dec. 2018.

[28] K.P. Harrig et al. "Neutron Spectroscopy for pulsed beams with frame overlap using a double time-of-flight technique". In: *Nuclear Instruments and Methods in Physics Research Section A: Accelerators, Spectrometers, Detectors and Associated Equipment* 877 (2018), pp. 359–366. ISSN: 0168-9002. DOI: https://doi.org/10.1016/j.nima.2017.09.051. URL: https://www.sciencedirect.com/science/article/pii/S0168900217310215.

[29] S. Hilaire and S. Goriely. "Towards More Predictive Nuclear Reaction Modelling". In: *Proceedings of the 6th International Workshop on Compound-Nuclear Reactions and Related Topics* 254 (2018), pp. 3–15.

[30] *Huepar 902CG - Self-Leveling 360-Degree Cross Line Laser Level with Pulse Mode and Magnetic Pivoting Base*. https://uk.huepar.com/products/huepar-902cg-self-leveling-360-degree-cross-line-laser-level-with-pulse-mode-switchable-horizontal-and-vertical-green-beam-laser-tool-magnetic-pivoting-base-included. Hueper. 2024.

[31] A.M. Hurst et al. "The Baghdad Atlas: A relational database of inelastic neutron-scattering (n,n'γ) data". In: *Nuclear Instruments and Methods in Physics Research Section A: Accelerators, Spectrometers, Detectors and Associated Equipment* 995 (2021), p. 165095. ISSN: 0168-9002. DOI: https://doi.org/10.1016/j.nima.2021.165095. URL: https://www.sciencedirect.com/science/article/pii/S0168900221000796.

[32] T. Kawano. "CoH_3: The Coupled-Channels and Hauser-Feshbach Code". In: *Proceedings of the 6th International Workshop on Compound-Nuclear Reactions and Related Topics* 254 (2018), pp. 27–34.

[33] M. Kireeff Covo et al. "The 88-Inch Cyclotron: A one-stop facility for electronics radiation and detector testing". In: *Measurement* 127 (2018), pp. 580–587. ISSN: 0263-2241. DOI: https://doi.org/10.1016/j.measurement.2017.10.018. URL: https://www.sciencedirect.com/science/article/pii/S0263224117306401.

[34] Leo E. Kirsch et al. "A new measurement of the ^{6}Li(n,α)t cross section at MeV energies using a ^{252}Cf fission chamber and ^{6}Li scintillators". In: *Nuclear Instruments and Methods in Physics Research Section A: Accelerators, Spectrometers, Detectors and Associated Equipment* 874 (2017), pp. 57–65. ISSN: 0168-9002. DOI: https://doi.org/10.1016/j.nima.2017.08.046. URL: https://www.sciencedirect.com/science/article/pii/S0168900217309464.

[35] Z. Kis et al. "Comparison of efficiency functions for Ge gamma-ray detectors in a wide energy range". In: *Nuclear Instruments and Methods in Physics Research Section A: Accelerators, Spectrometers, Detectors and Associated Equipment* 418.2 (1998), pp. 374–386. ISSN: 0168-9002. DOI: https://doi.org/10.1016/S0168-9002(98)00778-5.

[36] Glenn F. Knoll. *Radiation Detection and Measurement*. 111 River Street, Hoboken, NJ 07030: John Wiley & Sons, 2010.

[37] P. E. Koehler. "^{35}Cl(n,p)^{35}S cross section from 25 meV to 100 keV". In: *Phys. Rev. C* 44 (4 Oct. 1991), pp. 1675–1678. DOI: 10.1103/PhysRevC.44.1675. URL: https://link.aps.org/doi/10.1103/PhysRevC.44.1675.

[38] Kenneth S. Krane. *Introductory Nuclear Physics*. 111 River Street, Hoboken, NJ 07030: John Wiley & Sons, 1988.

[39] S. A. Kuvin et al. "Nonstatistical fluctuations in the ^{35}Cl$(n,p)^{35}$S reaction cross section at fast-neutron energies from 0.6 to 6 MeV". In: *Phys. Rev. C* 102 (2 Aug. 2020), p. 024623. DOI: 10.1103/PhysRevC.102.024623. URL: https://link.aps.org/doi/10.1103/PhysRevC.102.024623.

[40] Paul W. Lisowski and Kurt F. Schoenberg. "The Los Alamos Neutron Science Center". In: *Nuclear Instruments and Methods in Physics Research Section A: Accelerators, Spectrometers, Detectors and Associated Equipment* 562.2 (2006). Proceedings of the 7th International Conference on Accelerator Applications, pp. 910–914. ISSN: 0168-

9002. DOI: https://doi.org/10.1016/j.nima.2006.02.178. URL: https://www.sciencedirect.com/science/article/pii/S0168900206003792.

[41] R. G. Littlejohn. *Central Force Motion*. Physics 221A/B Lecture Notes, 2021. URL: https://bohr.physics.berkeley.edu/classes/221/2122/221.html.

[42] R. G. Littlejohn. *Fine Structure*. Physics 221A/B Lecture Notes, 2021. URL: https://bohr.physics.berkeley.edu/classes/221/2122/221.html.

[43] R. G. Littlejohn. *Introduction to Time-Independent Scattering Theory and Scattering from Central Force Potentials*. Physics 221A/B Lecture Notes, 2021. URL: https://bohr.physics.berkeley.edu/classes/221/2122/221.html.

[44] R. G. Littlejohn. *The Lippmann-Schwinger Equation and Formal Scattering Theory*. Physics 221A/B Lecture Notes, 2021. URL: https://bohr.physics.berkeley.edu/classes/221/2122/221.html.

[45] Michael Martin et al. "Feasibility of a Breed-and-Burn Molten Salt Reactor". In: *Transactions of the American Nuclear Society* 116 (July 2017). ISSN: 0003-018X. URL: https://www.osti.gov/biblio/23050349.

[46] T. Martinez et al. "Characterization of a CLYC detector for underground experiments". In: *Nuclear Instruments and Methods in Physics Research Section A: Accelerators, Spectrometers, Detectors and Associated Equipment* 906 (2018), pp. 150–158. ISSN: 0168-9002. DOI: https://doi.org/10.1016/j.nima.2018.07.087. URL: https://www.sciencedirect.com/science/article/pii/S016890021830932X.

[47] Seth McConchie et al. *Assessment of Modeling and Nuclear Data Needs for Active Neutron Interrogation*. Tech. rep. ORNL/TM-2021/1900. Oak Ridge National Laboratory, Apr. 2021. DOI: 10.2172/1778086. URL: https://www.osti.gov/biblio/1778086.

[48] P.S. Prusachenko and T.L. Bobrovskiy. "Features of using Cs2LiYCl6:Ce based scintillation detector for time-of-flight application". In: *Nuclear Instruments and Methods in Physics Research Section A: Accelerators, Spectrometers, Detectors and Associated Equipment* 1056 (2023), p. 168582. ISSN: 0168-9002. DOI: https://doi.org/10.1016/j.nima.2023.168582. URL: https://www.sciencedirect.com/science/article/pii/S0168900223005727.

[49] D. Radford. *RadWare*. https://radware.phy.ornl.gov. Accessed 12 January 2024.

[50] P. Ring and P. Schuck. *The Nuclear Many-Body Problem*. Berlin Heidelberg: Springer, 2004.

[51] A. Ruben et al. *A New, Versatile, High-performance Digital Pulse Processor with Application to Neutron/Gamma-Ray Pulse-Shape Discrimination in Scintillator Detectors*. July 2018. DOI: 10.13140/RG.2.2.14187.18727.

[52] G. R. Satchler. *Introduction to Nuclear Reactions*. New York: John Wiley and Sons, 1980.

[53] *Silicone Rubber Optical Interface EJ-560*. Accessed 5 amrch 2024. Eljen Technology. 2021. URL: https://eljentechnology.com/products/accessories/ej-560.

[54] D.L. Smith and N. Otuka. "Experimental Nuclear Reaction Data Uncertainties: Basic Concepts and Documentation". In: *Nuclear Data Sheets* 113.12 (2012). Special Issue on Nuclear Reaction Data, pp. 3006–3053. ISSN: 0090-3752. DOI: https://doi.org/10.1016/j.nds.2012.11.004. URL: https://www.sciencedirect.com/science/article/pii/S0090375212000907.

[55] Martin B. Smith et al. "Fast Neutron Spectroscopy Using $Cs_2LiYCl_6 : Ce$ (CLYC) Scintillator". In: *IEEE Transactions on Nuclear Science* 60.2 (2013), pp. 855–859. DOI: 10.1109/TNS.2012.2219068.

[56] J. Suhonen. *From Nucleons to Nucleus: Concepts of Microscopic Nuclear Theory*. 233 Spring Street, New York, NY 10013: Springer, 2007.

[57] J. R. Taylor. *An Introduction to Error Analysis: The study of uncertainties in physical measurements*. 55D Gate Five Rd. Sausalito, CA 94965: University Science Books, 1997.

[58] TerraPower. *TerraPower's Molten Chloride Fast Reactor Technology: Nuclear for a Changing Energy Sector*. https://www.terrapower.com/wp-content/uploads/2023/03/TP 2023 MCFR Technology-0216.pdf. 2023.

[59] T. Yamazaki. "Tables of coefficients for angular distribution of gamma rays from aligned nuclei". In: *Nuclear Data Sheets. Section A* 3.1 (1967), pp. 1–23. ISSN: 0550-306X. DOI: https://doi.org/10.1016/S0550-306X(67)80002-8. URL: https://www.sciencedirect.com/science/article/pii/S0550306X67800028.

[60] Hugh D. Young and Roger A. Freedman. *University Physics*. 1301 Sansome St. San Francisco, CA 94111: Pearson Education Inc., 2008.

[61] Yu. P. Popov and F. L. Shapiro. "The Cl-35(n,p) reaction and neutron resonance parameters of chlorine". In: *Sov. J. Nucl. Phys* 13 (1961), p. 1132.